12-15-2014

Quantitative Comparison of Time-Frequency Decomposed Gait EMG Signals

L. Patrick Mitchell
University of South Carolina - Columbia

Quantitative Comparison of Time-Frequency Decomposed Gait EMG Signals

by

L Patrick Mitchell

Bachelor of Science
University of South Carolina 2008

Master of Engineering
Yonsei University 2013

Submitted in Partial Fulfillment of the Requirements

for the Degree of Doctor of Philosophy in

Electrical Engineering

College of Engineering and Computing

University of South Carolina

2014

Accepted by:

Yong-June Shin, Major Professor

Roger Dougal, Committee Member

Charles Brice, Committee Member

Debra Krotish, Committee Member

Lacy Ford, Vice Provost and Dean of Graduate Studies

Dedication

To Ralph M. Leslie

May I be a man of integrity, who lived a life worth remembering

1924-2014

Acknowledgments

When mankind takes it upon itself to learn, it must be first humble to recognize and appreciate those whose footsteps precede its journey. I would first like to thank the University of South Carolina College of Engineering and Computing, for its role in my development as a professional and as a person. There are many professors who have changed me and afforded me the impetus to learn.

I would like to specifically thank Dr. Roger Dougal, Dr. Antonello Monti, and Dr. Charles Brice for their challenging courses and their friendships to me as I have progressed. Next I would like to thank Yonsei University for the opportunity to study there and be immersed in a culture a world away from my South Carolina home. A special thank you to Dr. Hur, Dr. Che, my master's degree committee, without whose support I would not be where I am today.

Next, I owe a great deal of gratitude to Dr. Debra Krotish, whose foresight, collaboration, knowledge, and friendship have been, and continue to be, a boon for which I am grateful. For all this, my journey has been made possible by Dr. Yong-June Shin, whose excellence and determination have crafted me into a man I can be proud of. Finally, I would like to thank my parents, my friends, my colleagues at both USC and Yonsei University, and all those who have walked beside me on my journey.

L Patrick Mitchell

The University of South Carolina

May 2014

Abstract

Falls in the senior population represent an immediate threat to both current and future generations' quality of life. The results of falls can be disastrous, create a long road to recovery, and in many cases result in death. Hypertension represents a difficult-to-quantify condition which is known to contribute to gait and balance dysfunction. Accurate assessment of conditions such as these represents an area of primary investigative need.

In order to meet this need, a new experimental setup is developed which combines time-frequency analysis with surface electromyography (sEMG) signals obtained during ambulation. 3-bit pressure data is acquired using a pressure-sensitive mat, which records time-aligned gait information alongside 8 dipole sEMG sensors attached to tibialis anterior, gastrocnemius, biceps femoris and vastus lateralis. These muscles serve as representative muscles for the ankle flexor, calf (knee flexor), hamstring and quadriceps groups. In all muscles save the biceps femoris, these represent largest muscle in each respective group, providing a comprehensive picture of muscular activation during gait.

The sEMG signals are recorded simultaneously with those of a pressure-sensitive mat, the data from which is used to identify the sinusoidal center of mass for gait separation. The two signals are time-aligned using a recording trigger sent from a standalone digital output device. Signals are imported into MATLAB and rejected according to Grubb's test using $\beta = 90\%$ on each of three signal attributes: signal energy, signal dc level, signal and peak-to-peak voltage. Signals are decomposed using a Hann window reduced interference distribution, with an $N_t = 53$-point Hann time

window and $N_\omega = 96$-point Blackmann frequency window.

Six metrics based on the physiology and spectral analysis of sEMG signals are used to evaluate and compare several population groups. These metrics are: Instantaneous time duration($TD_\%$), local frequency bandwidth (F_B), local frequency maximum (F_{max}), energy ratio conditional (E_{ω_b}), conditional energy from 40-100 Hz ($E\%_{40-100Hz}$), and energy spectral density from 40-100 Hz ($ESD_{40-100Hz}$). These metrics rely on both Fourier transform spectrum distributions and accurate time-frequency localized distributions.

Using a large subject database, 10 male and 20 female controls are compared to 7 male and 17 female hypertensive subjects across the six metrics. Subjects are separated into control and experimental groups using medical history and self-report data; age was not a factor. Each of the six metrics are then evaluated in the four muscle groups for differentiability between control and experimental groups. These metrics are then evaluated in male and female subgroups.

In the male subgroup, when using the tibialis anterior muscle, $TD_\%$, F_B, and $E_{\omega_b=120Hz}$ showed a maximal accuracy of 75.00%, 76.92% and 76.92% respectively. In the gastrocnemius, both F_B and $E_{\omega_b=120Hz}$ showed 76.92% accuracy. In the vastus lateralis, F_{max}), and $E_{\omega_b=120Hz}$ showed 76.92% accuracy, while $E_{\omega_b=40Hz}$ showed 75.00% accuracy. The biceps femoris showed low levels of accuracy (maximum 62.50%).

In the female subgroup, the overall level of accuracy is lower, due to physiological factors of subcutaneous tissue, muscle distribution, and gait differences. In the tibialis anterior, $E_{\omega_b=40Hz}$ showed the highest accuracy at 68.42%, with $TD_\%$ at 66.67%. In the gastrocnemius, $TD_\%$ showed highest accuracy. In the vastus lateralis, $E_{\omega_b=120Hz}$ showed the highest accuracy, and in the biceps femoris, $E_{\omega_b=40Hz}$ showed the highest level of accuracy.

Using an aggregate of these key metrics, an accuracy of 94.12% for male subsets and 78.38% for female subsets is established for testing control groups vs hypertensive

experimental groups. This research represents a hypertension diagnostic tool, and thus a quantitative indicator of fall risk.

Table of Contents

Dedication ii

Acknowledgments iii

Abstract iv

List of Tables ix

List of Figures x

Chapter 1 Introduction 1

1.1 Signal Processing 1

1.2 Electromyography 2

1.3 Motivations 6

Chapter 2 Time-Frequency Analysis 9

2.1 Fourier Transform 10

2.2 Description of Signals 13

2.3 Short-Time Fourier Tranform 15

2.4 Cohen's Class of Time-Frequency Kernels 22

2.5 Summary 25

Chapter 3 Physiology 27

3.1 Muscular Model 27

3.2 Surface EMG Measurement 29

3.3 Surface EMG Signal Interpretation 30

3.4 Gait 34
3.5 Muscle Selection 35
3.6 Summary 40

Chapter 4 Experimental 42
4.1 Data Acquisition and Setup 42
4.2 Footfall Separation by Gait-Sine Algorithm 45
4.3 Database Subsets 49
4.4 Data Pre-Treatment 51
4.5 Application of Time-Frequency Analysis 54
4.6 Metric Design 56
4.7 Summary 61

Chapter 5 Results 63
5.1 Statisitcal Evaluation 63
5.2 Male Control vs Male Hypertensive 66
5.3 Female Control vs Female Hypertensive 69
5.4 Discussion 71

Chapter 6 Conclusion 74

Bibliography 77

List of Tables

Table 4.1 Gait cycle activation by muscle with appropriate gait-sine parallel 49

Table 4.2 Metrics summary 56

Table 5.1 Metric and muscle values for male subsets 67

Table 5.2 Metric and muscle values for female subsets 70

List of Figures

Figure 1.1 Diagram of frog muscle contraction measurement experiment of Emil du Bois-Reymond 3

Figure 1.2 Total medical costs of unintentional fall-related injuries in United States senior populations by sex and age in 2005 [26] 7

Figure 2.1 Time-domain waveform of musical arrangement example 10

Figure 2.2 Single-sided power spectrum of musical segment example from $1Hz$ to $10kHz$ 12

Figure 2.3 Single-sided power spectrum of 10-point decimated musical segment example from $1Hz$ to $1kHz$ with key frequency points marked 13

Figure 2.4 Rectangular windowed clip of 71 ms from musical time-series example 18

Figure 2.5 Hamming windowed clip of 71 ms from musical example 19

Figure 2.6 Time-aligned (a) time-frequency distribution and (b) musical notation of musical example 22

Figure 2.7 Wigner-Ville distribution with spectrum and time domain signal displayed alongside time- and frequency-aligned axes for musical example 24

Figure 2.8 Hann Window RID with spectrum and time domain signal displayed alongside time- and frequency-aligned axes for musical example 25

Figure 3.1 Diagram of muscle signaling from (a) spinal cord, (b) neuron cell body (c) spinal nerve, (d) nerve fiber, and (e) termination at muscle fiber [10] 28

Figure 3.2 Diagram for sEMG signal acquisition, with (a) expanded system-level interpretation of muscle firing summation with (b) individual motor unit firings, (c) varied subcutaneous filters, and (d) summation at skin surface; Acquisition by (e) sEMG sensors with (f) electrical distant ground feeding (g) differential amplifier, (h) filtered using band-pass rejection results in (i) final sEMG signal 29

Figure 3.3 Graph of relevant force and temporal effects on power density spectrum 32

Figure 3.4 Leg muscle diagram indicating location of (a) vastus lateralis, (b) tibialis anterior, (c) gastrocnemius, and (d) biceps femoris muscles 36

Figure 3.5 Gait cycle aligned with normalized EMG voltages of (a) vastus lateralis, (b) tibialis anterior, (c) gastrocnemius, and (d) biceps femoris muscles 37

Figure 4.1 Diagram for experimental setup with (a) belt-worn sEMG transmitter unit, (b) sEMG sensors connected to muscles, (c) wi-fi receiver with example sEMG signal, (d) data recording computer, (e) walkway data converter, (f) pressure-sensitive walkway with example footfall pressure signal 43

Figure 4.2 3-dimensional graph of center of mass during gait, with (a) lateral and (b) vertical directions with (c) lemniscate pattern shown; image adapted from [47] 46

Figure 4.3 Walk recording of subject 015 with pressure summation and superimposed best fit sinusoid shown 47
Figure 4.4 (Repetition of Figure 3.5) Gait cycle aligned with normalized EMG voltages of (a) vastus lateralis, (b) tibialis anterior, (c) gastrocnemius, and (d) biceps femoris muscles 48
Figure 4.5 Subject 091, left and right tibialis anterior EMG with Gait-Sine estimate, muscle activation bounded by box 50
Figure 4.6 Diagram of population demographics for controls (P_0), shown as green, and hypertensives (P_1), shown as red, subdivided by age with number of subjects (N), mean age ($\overline{age}$) and variance (σ) shown 51
Figure 4.7 DC levels for male hypertensive-control subgroup walks with rejected sEMG data marked by x 53
Figure 4.8 Time-frequency distribution including energy spectral density and time-domain waveforms 57

Figure 5.1 Flowchart for assessment of metric sensitivity between populations 66
Figure 5.2 Histogram of aggregated metric scores for female control vs hypertensive, by confusion matrix score 68
Figure 5.3 Aggregated metric scores by subject number, controls represented by green, hypertensives represented by blue, with error bars corresponding to $\pm\frac{\sigma}{2}$ for aggregate score, x axis 'y' refers to young control, 's' refers to senior control, 'e' refers to experimental 69

Chapter 1

Introduction

1.1 Signal Processing

Signal processing is a robust field which allows both the creation and investigation of a variety of signals. For example, while humans have been singing since before recorded history, signal processing allows for the perfection and manipulation of pitch, tone, and tempo. In space, radio waves carry information about dying stars and black holes, allowing glimpses into the beginnings of the universe. Satellites transmit information across the Earth at rates which surpass the understanding of every generation before. Even the human central nervous system serves as a beacon for the brain, transmitting information on muscle action by way of electrical impulses. Signal analysis therefore provides a tool with which to examine a wide array of information.

In order to translate the information a signal carries into comprehensible terms, they must often be transformed into domains which are already understood. One of the earliest mathematical tools for signal transformation was developed by Joseph Fourier [1], from his work on heat transfer. His major contribution is a transformation which takes a function of time and translates it into a function of frequency through the use of a sine-wave summation. This transform then allowed for new analysis of known functions, and the relationship between time and frequency. Thus, a signal that might have little meaning in the time domain might be better understood as a function of frequency.

While signals which repeat perfectly at some fundamental frequency are easy to transform into frequency representations, many signals acquired directly from real-world proceses do not exhibit this property. For example, signals such as speech, music, television, and others are non-stationary, and change in frequency content from moment to moment. Thus, while Fourier's transform is useful in many cases, it was inadequate to analyze the time-varying frequency content of the signals.

Consequently, there was a clear need for a methodology which could describe energy as a function of both frequency and time. The first such transform was proposed by Ville [2], and later improved by Wigner. This process allowed direct calculation of energy from joint time and frequency moments. And so, time-frequency analysis provides a way to interpret a transient phenomenon which contain time- and frequency- information in a joint manner.

However, this so-called Wigner distribution was sensitive to cross-term distortion from the inherent mathematical expression. Hence, other time-frequency distributions, with alternative desirable qualities, were conceptualized and investigated. These kernels were designed with reduced interference in mind [3], after being summarized for a general case [4]. Hence, time-frequency analysis has become a tool for describing a myriad of signals, whose information had been masked by their transience. These concepts are extended mathematically in chapter 2. In this work, these signal processing tools are used to decompose and analyze signals acquired through electromyography.

1.2 Electromyography

Electromyography (EMG), or the study electrical signals generated by muscles during contraction, has enjoyed a long and beautiful history of discovery. The electricity-muscle relationship was first hypothesized and investigated by Francesco

Redi, during his work on the electric eel. This was expanded later by Walsh [5], who recognized that contraction could create electricity, and vice-versa by Galvani [6], [7], when he used elecctricity to depolarize frog legs. Galvani's findings were investigated by Volta [8], who identified several inconsistencies which were later replaced by more accurate theories. These advances culminated in the work of Emil du Bois-Reymond [9], who is recognized as the father of neurology.

The investigation and ideas that du Bois-Reymond put forward were filled in over time, as the mechanisms behind the muscles were discovered through chemistry, biology, and engineering. The major contribution of du Bois-Reymond was the clear generation of electrical signals by the muscles, as well as the discovery of surface impedance of the skin, using a bullfrog connected to electrodes to stimulate a galvanometer. A diagram of this setup is shown in Figure 1.1. His experiment culminated in inducing blisters to reduce resistance [10], but through his dedication, the field was born.

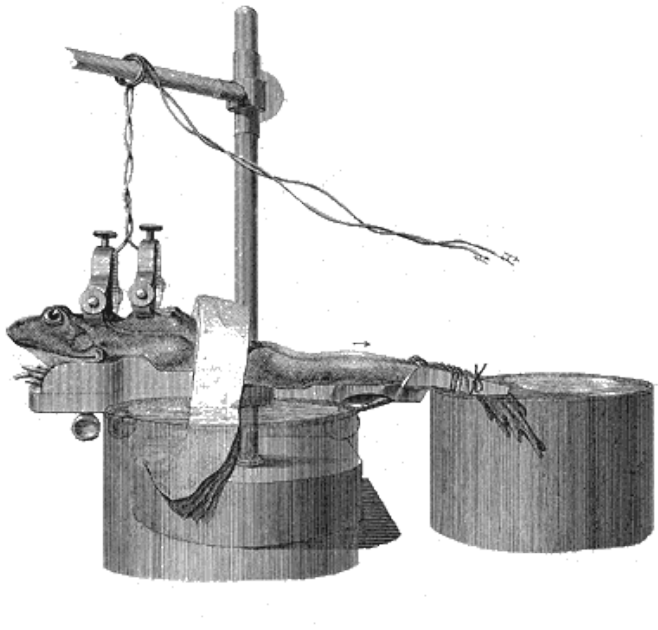

Figure 1.1: Diagram of frog muscle contraction measurement experiment of Emil du Bois-Reymond

Through the next century, the knowledge of the human central nervous system and its electrical implications continued to expand. The introduction of the amplifier using vacuum tubes, combined with the invention of the surface electrode allowed for much stronger stimulation of measurement devices during muscle contraction. Gasser and Erlanger [11] earned a Nobel Prize in 1944 by removing the inertia-based measurement systems and using tube-based amplification to drive an oscillograph, finally allowing an accurate representation of the low-voltage signals which drove muscular activation. They, like du Bois-Reymond, sampled from a frog's muscles, though because of the lack of inertia of a galvanometer, the recorded waveforms gave much better insight to the inner workings of muscular activation, especially how the signals varied over time.

After the invention of the silver/silver chloride surface electrode, the clinical and practical aspects of electromyography started to become apparent. One of the earliest exciting advances came when Russian scientists built a functioning prosthetic arm [12], which used surface electrodes connected to an amputee stump to actuate a claw. Since then, surface electromyography (sEMG) has progressed to new levels of integration in the clinical and outpatient worlds.

Many advances in sEMG technology have focused heavily on the relationship between muscle force and sEMG amplitude and frequency. In one case, fuzzy theory [13], was used to evaluate sEMG signals taken during weightlifting. Upon comparison to the actual amount of weight lifted, a highly accurate assessment of force was made using the Fourier-transformed raw sEMG signals. Staudenmann et al. [14], [15] developed a unique protocol for assessment of entire motor units using a high-density grid of electrodes. By using this grid, they could evaluate various configurations of electrodes, and achieved optimal results for evaluation of the force level using principal component analysis. Thus, sEMG represents a dependable tool for assessment of muscular force.

Additionally, sEMG signals can be used to directly assess complex presentations of muscular malfunction, where it may be difficult to tease out specific diagnoses simply from the symptoms. Muscular degeneration has a variety of causes, such as carpal tunnel [16] or thyroid dysfunction [17], but sEMG may be used to adequately asses these causes. This ability allows sEMG signal analysis a privileged position, with its ability to tease out underlying information.

Because of this fact, one area sEMG is uniquely suited for is that of human gait analysis. EMG signals during ambulation give indications of gait abnormalities, and can help in the assessment of underlying causes. Additionally, the ability of sEMG to assess group motor function has been exploited to determine gait cycle during ambulation under changing conditions [18], which can be used by extension to assess gait patterns. However, gait represents a complex, time-dependent signal for which additional tools are necessary. To meet the need for assessing the time-dependent instantaneous frequency over each gait cycle, time-frequency analysis is used.

Time-frequency analysis has long shown itself an effective tool non-stationary signal analysis, especially within the medical field. Through applying time-frequency analysis, conditions such as muscle fatigue [19] or Parkinson's [20] may be quantified. Electroencephalogram signals, based on the same underlying principles as sEMG signals, have been used to successfully decompose and identify seizures in newborns [21], [22]. Because the key wavelengths in EEG signals vary by frequency, time-frequency analysis can serve as a useful indicator for the detection and elimination of artifacts from the signals [23]–[25].

Thus, sEMG signals, evaluated using time-frequency analysis, become useful tools for assessment of time-dependent signals, such as during ambulation. These tools may be applied to areas in need of investigation, such as that of fall risk assessment in this dissertation.

1.3 Motivations

As modern medicine has advanced, the average age of passing has steadily increased, leading to new needs within the medical community. One of the primary risks to the quality of life in senior populations is the risk of falling. Falls are also associated with a much higher risk of mortality in seniors [27], besides the clear psychological effects of loss-of-independence associated with falls. Falling is a problem for not just the senior community, as an estimated $19.5 billion dollars of health care costs in the United States in 2000 [28] were attributed, directly and indirectly, to falls. Meanwhile, for seniors, the risk and cost of hospitialization rises with age. The CDC reports [26] from 2005 on the cost of falls to seniors are shown in Figure 1.2. Figure 1.2(a) shows the cost in millions of dollars for those seniors who are released, while Figure 1.2(b) shows the cost of those who are hospitalized. As seniors age, the cost of fall-related injury increases, and as the senior population increases, the number of fall-related injuries and deaths are also likely to increase. Thus, conditions which affect fall risk are of prime investigative need, especially if they can be identified early on, to minimize the economic impact of falls.

Falls and fall risk, like ambulation, are complex and multivariable manifestations of complex underlying factors. However, some of the primary factors for fall risk are well-understood. The condition of the musculature, such as muscular mass, strength, and power, have been shown to significantly affect fall risk [29]. Additionally, leg power [30] has been shown to correlate with fall risk. Thus, sEMG's usefulness in this area is already well-established. Additionally, several comorbidities have been associated with increased fall risk. Hypertension [31] has been shown as a link between increased risk of falling, though the quantification of this relationship is difficult. Thus, sEMG can serve an important role in quantifying key factors in fall risk assessment.

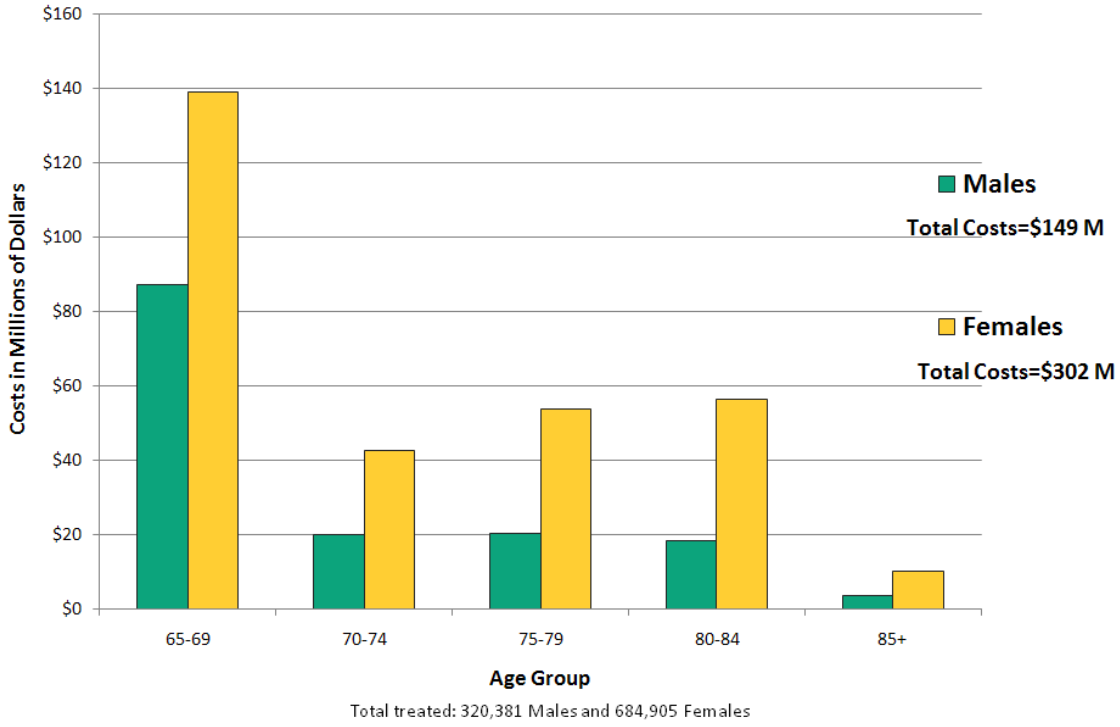

(a) Treated and released

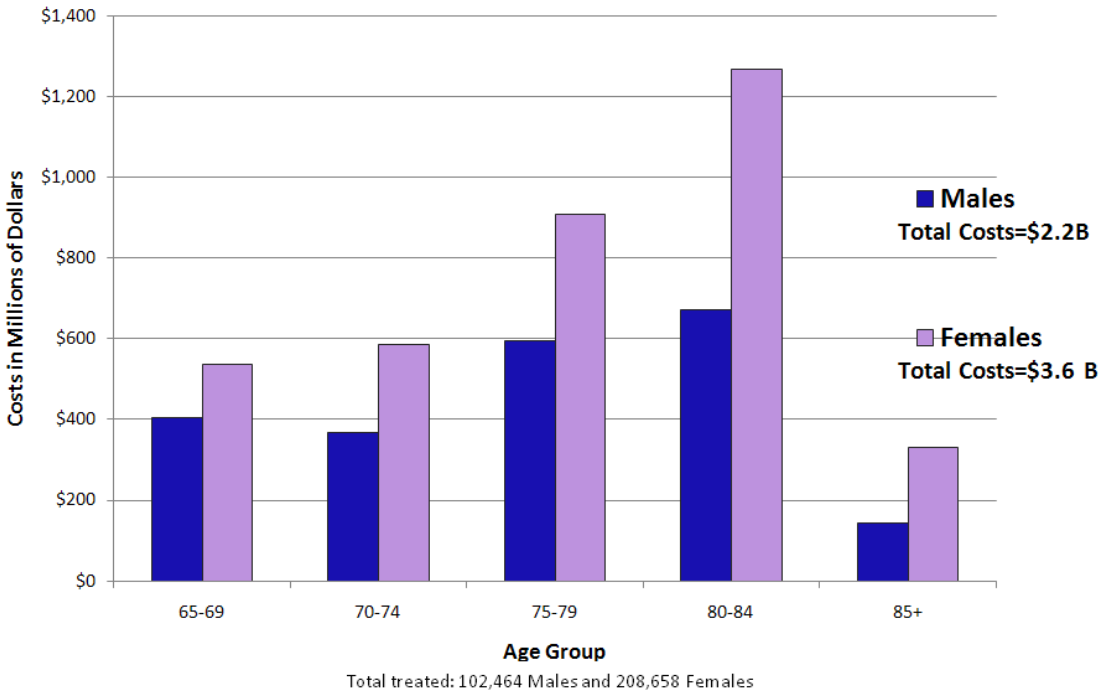

(b) Treated and hospitalized

Figure 1.2: Total medical costs of unintentional fall-related injuries in United States senior populations by sex and age in 2005 [26]

Hypertension presents a uniquely difficult-to-quantify condition, due to masking direct evaluation of its effects when a patient is undergoing treatment. However, the effects of hypertension on gait exist as a symptom even in patients being treated for hypertension [31]. Thus, the effects of hypertension may be quantified using sEMG signals during gait.

In this initial research, a non-longitudinal observational study was performed in order to evaluate the efficacy of detecting the presence of hypertension using sEMG signals. Hypertension was chosen as a control variable due to its difficult-to-quantify nature, and common presence among seniors. This research may be expanded in the future to a full longitudinal study in order to evaluate the link between hypertension and fall risk directly from the gait sEMG data.

In this dissertation, the first two chapters serve to inform the background knowledge which is requisite for understanding both the experimental design and results. Ch. 2 develops the mathematical concepts behind time-frequency analysis, from the Fourier transform on to Cohen's class of time-frequency transforms. Ch. 3 explains the underpinnings of sEMG in the context of gait, as well as the effects of physiology on the signals observed at the point of contact. Ch. 4 explains the experimental setup used, as well as the design of metrics to evaluate changes in gait sEMG signals. Finally, these metrics are categorized using statistical methodologies to evaluate differences between populations in Ch. 5.

Chapter 2

Time-Frequency Analysis

In order to properly contextualize the use of signal processing in this dissertation, the tools used must be fully understood. In this Chapter, the mathematical background which underpins time-frequency analysis are investigated. The mathematical tools that time-frequency analysis provides is used to distill the large amount of information acquired through the experiment, and to evaluate by comparison between groups. The concepts of time-frequency analysis will be explained by progressing through classical methods of signal analysis, such as the Fourier transform, and continuing on to time-frequency analysis through the use of a non-stationary musical arrangement.

First, the Fourier transform is explained, as well as its usefulness in evaluating frequency information in section 2.1. From here, several simplistic methods of signal analysis are explained in section 2.2, including bandwidth and time moments, which can be obtained directly from the time-domain signal or Fourier transform of the signal. These core concepts are extended to time-localized cases using the short-time Fourier transform (STFT) in section 2.3. Finally, this culminates in the definition of Cohen's class of time-frequency transforms, as defined by their various kernels and properties in section 2.4

Non-Stationary Signal Example: Musical Arrangement

As an example of a non-stationary signal, a small portion of a musical recording is used. This represents an extremely complex signal, as each instrument involved

creates various spectral content over a range of frequencies, including the fundamental and harmonics of all instruments involved. Furthermore, the instrument tone and fundamental pitch change over time. For this reason, a clip from Miles Davis' Blue in Green [32] is used, from time $t = 18s$ to $t = 26s$, which has only three instruments and minimal changes in fundamental frequencies. These 8.57 seconds represent eight beats in the music, which contain multiple frequency elements over a wide bandwidth. When the original signal is downsampled to $f_s = 4.41kHz$, the resulting time domain waveform, shown in Figure 2.1, shows several distinct amplitude changes over the window, which correspond to the sound produced by the piano and trumpet. This example will be used to illustrate the concepts of the following sections.

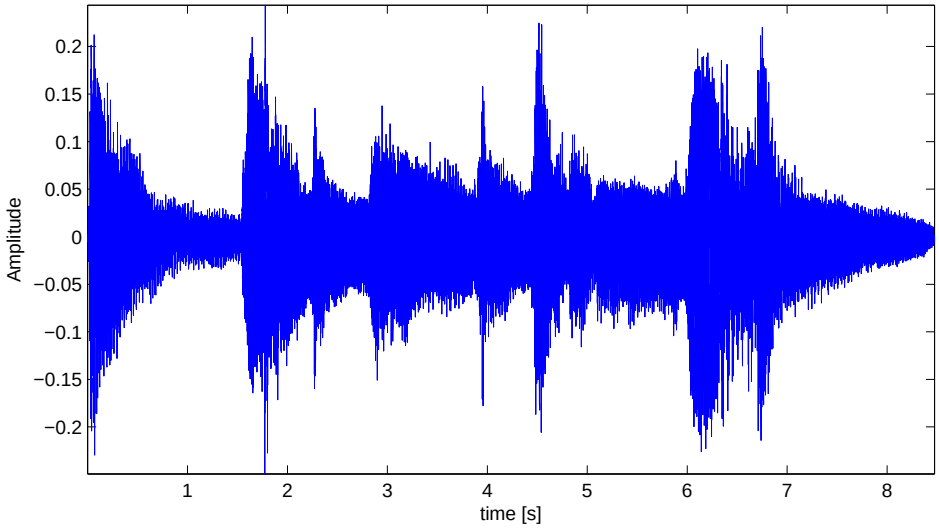

Figure 2.1: Time-domain waveform of musical arrangement example

2.1 Fourier Transform

One of the most powerful methods of interpreting signals recorded in the time domain is through the use of the Fourier transform. As explained in 1.1, Fourier's ideas came from his work on heat transfer, but the concepts can be extended to all periodic.

Translation of signals into the frequency domain results in new ways to interpret existing information. In the frequency domain, it is easier to evaluate a signal's cause, as well as the medium in which it operates, as these factors have clear influences on a signal's spectrum. This translation also simplifies our interpretation of multicomponent signals, such as instruments or voices, which may appear confusing in the time domain, but are simply combinations of weighted harmonics in the frequency domain. Additionally, the Fourier transform may provide the means for mathematical quantification of otherwise uninterpretable signals.

There are two incarnations of this transformation; one for continuous, infinite signals, and another for finite signals. For a signal, $s(t)$, the continuous Fourier transform takes the form

$$S(\omega) = \frac{1}{\sqrt{2\pi}} \int s(t) e^{-j\omega t} dt \tag{2.1}$$

Thus, the spectrum $S(t)$ is represented by the summation of sinusoidal waveforms $e^{j\omega t}$. To reconstruct the signal, these sinusoids are weighted by the spetrum point appropriate to their frequency:

$$s(t) = \frac{1}{\sqrt{2\pi}} \int S(\omega) e^{j\omega t} d\omega \tag{2.2}$$

A signal can then be interchanged in the time or frequency domains. This principle of energy conservation between the signals is known as Parsival's theorem:

$$E = \int |s(t)|^2 dt = \int |S(\omega)|^2 d\omega \tag{2.3}$$

where E is the total signal energy, and $|S(\omega)|^2$ is the energy density spectrum. The tools afforded by the Fourier transform may be used to describe key attributes of signals without significant computational burden.

Using the discrete Fourier transform, it is straightforward to determine the power spectrum representation of the example signal as the square of the transform. In

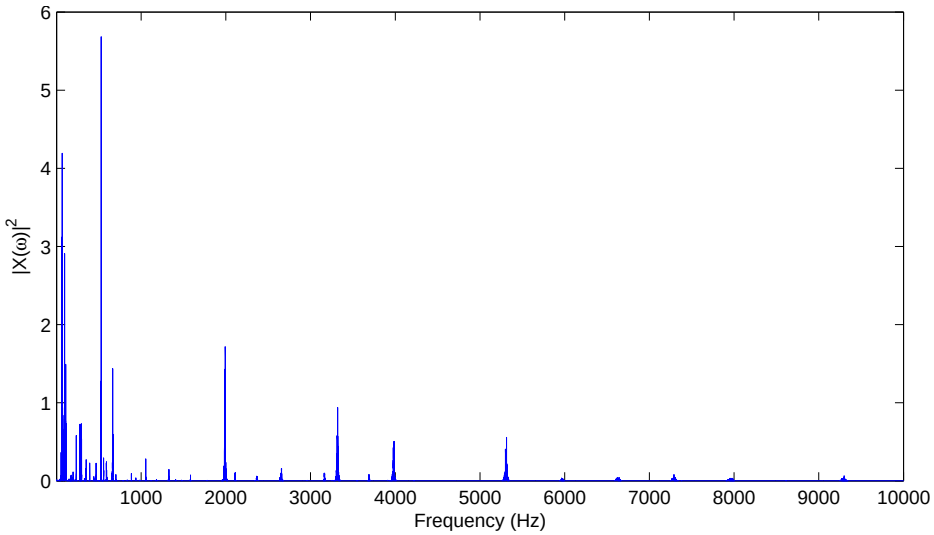

Figure 2.2: Single-sided power spectrum of musical segment example from $1Hz$ to $10kHz$

order to focus on the fundamental components, the spectrum is scaled from $1Hz$ to $10kHz$, and is shown in Figure 2.3.

In this representation, it is clear that a majority of the energy is concentrated below $1kHz$, in which the fundamental frequency components lie. However, the energy in the harmonics, at $2kHz$ and $3.3kHz$ contribute significantly to the overall energy. By decimating by a factor of ten, the fundamental components may be examined, as the relative sampling rate become $f_s = \frac{44.1kHz}{10} = 4.41kHz$, resulting in a Nyquist rate of $f_{Ny} = 2.21kHz$. This decimated spectrum from $1Hz$ to $1kHz$ is shown in Figure 2.3

Upon investigation of the decimated-signal spectrum, there seem to be three areas with high distributions of energy in the frequency domain. First, in the area of $60 - 108Hz$, a large concentration of energy can be seen. Next, in the area around $530Hz$, and finally, at $660Hz$. These points are identified using markers in Figure 2.3. However, it is not clear where these frequencies occur, as the signal itself is 8 seconds long. There are, however, other tools which may be helpful for the description of the signal.

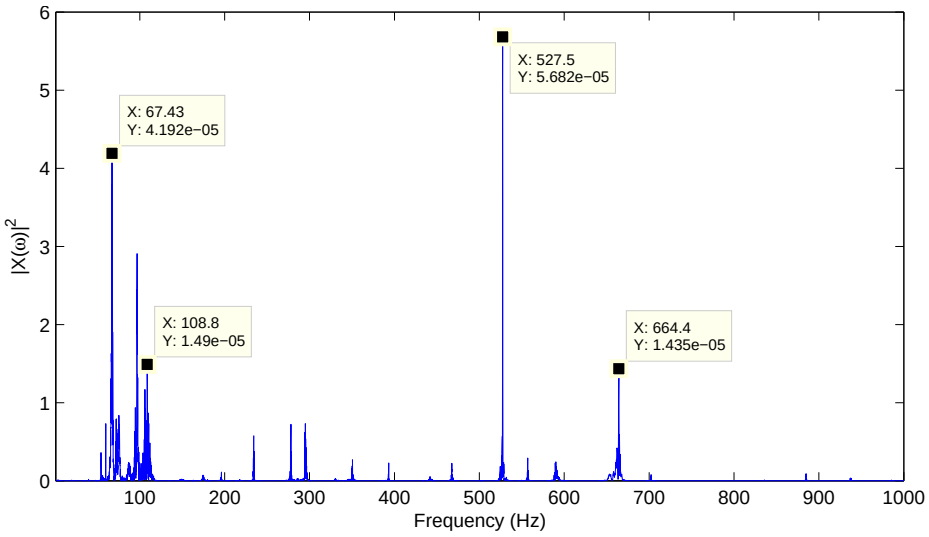

Figure 2.3: Single-sided power spectrum of 10-point decimated musical segment example from $1Hz$ to $1kHz$ with key frequency points marked

2.2 Description of Signals

The concept of moments in statistics is extremely useful, as it provides a straightforward interpretation of key descriptive variables for a function. In the case of signal processing, the time and frequency moments can be used to describe the mean and variance of a signal in either domains. For the n^{th} moment of a signal $s(t)$ in the time domain , the equation is given as:

$$\langle t^n \rangle = \frac{1}{E} \int t^n |s(t)|^2 dt \tag{2.4}$$

Thus, the first and second moments may be calculated by the use of (2.4) with n set at 1 and 2, respectively:

$$\langle t \rangle = \frac{1}{E} \int t |s(t)|^2 dt \tag{2.5}$$

$$\langle t^2 \rangle = \frac{4\pi}{E} \int t^2 |s(t)|^2 dt \tag{2.6}$$

These equations, (2.5) and (2.6), can then be used to calculate the variance, which gives an indication of the signal's breadth in time or frequency:

$$T^2 = \sigma_t^2 = \frac{4\pi}{E} \int (t - \langle t \rangle)^2 |s(t)|^2 dt \tag{2.7}$$

Additionally, the moments of the spectrum $S(\omega)$ can be used to evaluate the mean and variance of the frequency. These are given as:

$$\langle \omega \rangle = \frac{1}{E} \int \omega |S(\omega)|^2 d\omega \tag{2.8}$$

$$\langle \omega^2 \rangle = \frac{4\pi}{E} \int \omega^2 |S(\omega)|^2 d\omega \tag{2.9}$$

These equations, (2.8) and (2.9), are used in the calculation of the bandwidth, which is well-understood concept for describing the frequency content of the signal. The bandwidth corresponds to the standard deviation in the frequency domain, and is given by (2.10):

$$B^2 = \sigma_\omega^2 = \frac{4\pi}{E} \int (\omega - \langle \omega \rangle)^2 |S(\omega)|^2 d\omega \tag{2.10}$$

Using these sets of equations, it is straightforward to describe the decimated example signal in terms of its time and spectrum information. Using (2.5) , the time center for the musical signal is $\langle t \rangle = 4.05s$. Substituting into (2.7), a time spread of $T = 8.5s$.

From visual inspection of Figure 2.1, these values can be properly interpreted. The energy from $t = 3$ to $t = 5$ is extremely high, resulting in the first time-moment's skewness towards the beginning of the signal.

Extending to the frequency domain and using the spectrum as the probability distribution function results in $\langle f \rangle = 2.057kHz$ and a bandwidth of $B = 8.89kHz$. If using the 10-point decimated signal, the results are descriptive of the fundamental frequencies, rather than their harmonics. After evaluating the spectrum by the decimated signal (f_{deci}), the frequency center shifts to $\langle f_{deci} \rangle = 273.78Hz$. These values result in a bandwidth of $B_{deci} = 1.05kHz$.

These values are informative, but because of the long time duration of the signal, it is difficult to glean useful information about time-specific frequency changes. A fairly straightforward way to do this is through the STFT, which evaluates the frequency

spectrum of a small period of time, rather than an entire interval. This process, however, readily identifies the shortcomings of this method.

2.3 Short-Time Fourier Tranform

Several concepts are necessary to evaluate a non-stationary signal. First, the process of use of the analytic signal is explained, followed by the concept of windowing. These concepts will then allow for an explanation of the short-time Fourier transform and time-frequency kernels.

Analytic Signal

The first step in obtaining the time-aligned frequency content of a signal is to obtain the analytic version of that signal. Real-valued signals contain both positive and negative frequency elements at any given point, but by adding a known imaginary element, a mathematically complex signal can preserve phase information in a signal while eliminating the negative frequency elements, making numerous computations much more straightforward. Because of the Hermitian symmetry of a signal's spectrum, this results in no loss of information. This signal is known as the analytic signal, and it is obtained through the use of the Hilbert transform.

For a signal $s(t)$, the analytic signal $z(t)$ is obtained using the Hilbert transform, $H[s(t)]$. It takes the form [33]

$$H[s(t)] = \hat{s}(t) = \frac{1}{\pi} \int \frac{s(t')}{t - t'} dt' \tag{2.11}$$

Then the resulting analytic signal $z(t)$ may be expressed as a summation of the signal and the complex-shifted Hilbert-transformed signal $\hat{s}(t)$ as

$$z(t) = s(t) + j\hat{s}(t) \tag{2.12}$$

There are several reasons to use the analytic signal when producing time-frequency distributions. First, due to the symmetry of a non-analytic signal's spectrum around the origin, the average frequency would always be zero. This also results in difficulty calculating frequency spreading. Additionally, frequency and phase can be obtained from the analytic signal directly, since the first derivative of the signal $\hat{s}(t)$ represents the change in phase, or the frequency. Thus, the analytic signal represents a useful step towards a time-frequency distribution.

Windowing

A simple way to evaluate the frequency content of a time-localized portion of the signal is through the process of windowing. A windowed signal $\nu(\tau)$, centered at time τ takes the form

$$\nu(\tau) = \frac{s(\tau)h(\tau - t)}{\sqrt{\int |s(\tau)h(\tau - t)|^2 d\tau}} \tag{2.13}$$

The normalization ensures the energy in the windowed signal, $\int |\nu(\tau)|^2 d\tau = 1$, regardless of window size. This keeps the evaluation of the frequency content, regardless of window size or characteristic.

However, when the windowed signal is evaluated by the Fourier transform, the characteristics of the window $h(\tau)$ are imposed by the multiplication. Additionally, the window dimensions are constrained by the uncertainty principle, such that a small time window results in poor frequency localization, and a large time window gives a wider frequency bandwidth, to the detriment of the time-localization [34]. Thus, window selection and window length are of primary importance in effective evaluation of the time-dependent spectral content of a signal.

Window Selection

The first point for consideration is that of the window itself. Several windows exist which provide unique trade-offs between their own frequency- and time-localization

properties. The simplest window is that of the rectangular window, which does not alter the amplitude of the signal outside of the window bounds.

This is problematic for frequency evaluation, as the multiplication of a rectangular window with any original signal results in a much lower frequency resolution over the breadth of the discrete Fourier transform (DFT). This transformation results from low sideband reduction, and can be alleviated in a variety of ways. To illustrate this concept, consider Figure 2.4, which shows the time domain representation and respective spectrum representation for a $71ms$ portion of the musical example, taken at $t = 6.92s$. Notice the large number of side lobes present in the spectrum of Figure 2.4(b).

In order to overcome this problem, it is necessary to use a window which, when transformed to the frequency domain, does not produce so wide of a *sinc* function. One window which achieves this is the Gaussian window. The key property of the Gaussian function is that its Fourier transform is selfsame to its time-domain valuation, save for scaling. Thus, a window function based on the Gaussian function provides an equal trade-off between time and frequency domains, and minimizes the side-lobe aliasing.

A closely related set of windows rely on a raised cosine, known as the Hamming set of windows, which offer slightly better frequency evaluation, at the expense of time resolution [35]. This set is known as the Hamming class of windows, and take the form

$$h[n] = \alpha - \beta cos\left(\frac{2\pi n}{N-1}\right) \tag{2.14}$$

One effective valuation of the coefficients is that which reduces the magnitude of the first sideband. This incarnation is named after Hamming, and has coefficients of $\alpha = .54, \beta = 1 - \alpha = .46$. This elimination results in much better frequency resolution with respect to a small loss in time resolution. In order to see the effect that the Hamming window has on the same segment of the musical selection, consider

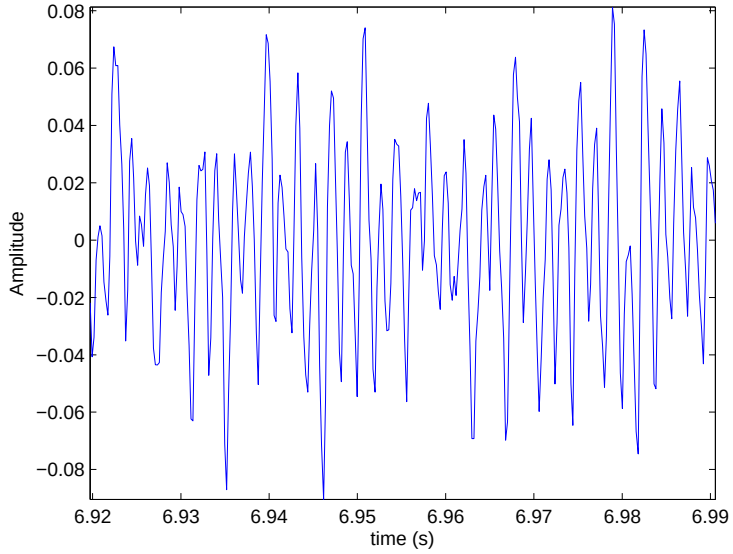

(a) Time domain

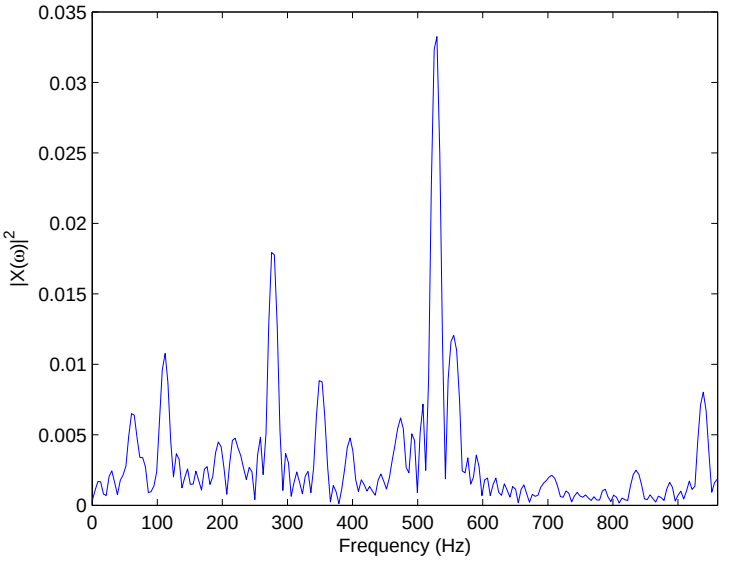

(b) Spectrum

Figure 2.4: Rectangular windowed clip of 71 ms from musical time-series example

Figure 2.5. The reduction in sideband aliasing causes the discrete Fourier transform to be much smoother, as is visible in Figure 2.5(b).

A final set of window families build on the Hamming window, but also include

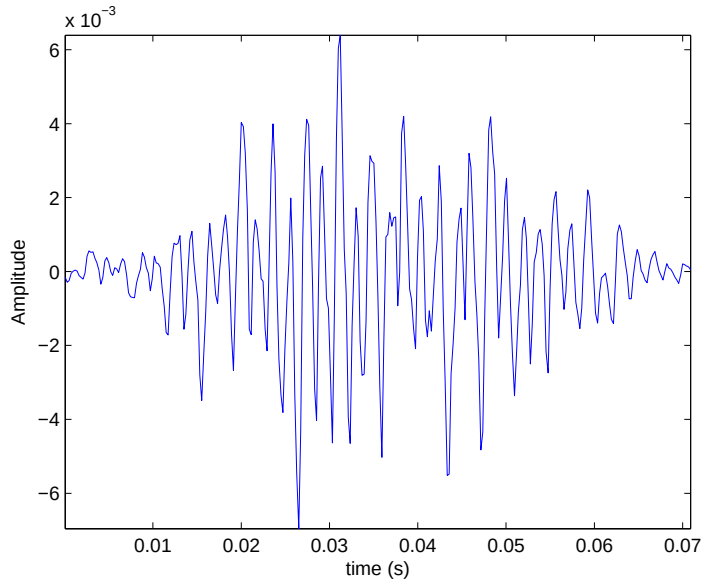

(a) Time domain

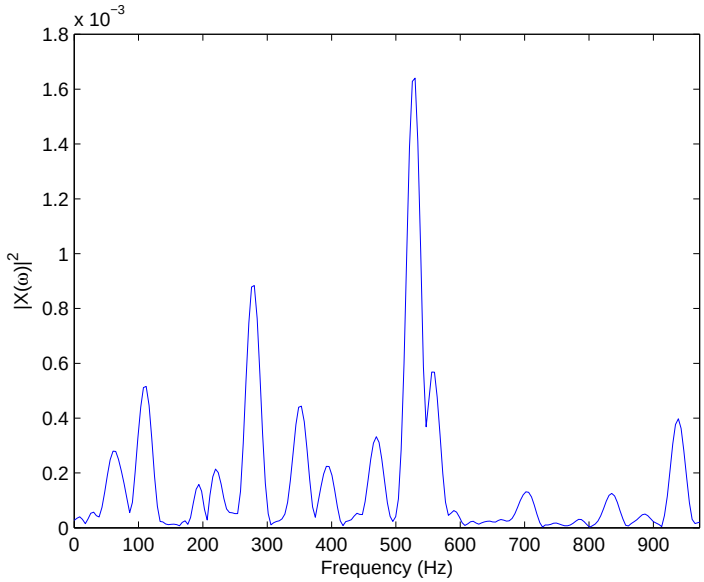

(b) Spectrum

Figure 2.5: Hamming windowed clip of 71 ms from musical example

higher-order harmonics of the cosine, and take the form

$$h[n] = \sum_{k=0}^{K} a_k cos\left(\frac{2\pi kn}{N}\right) \tag{2.15}$$

where

$$a_0 = \frac{1-\alpha}{2}; a_1 = \frac{1}{2}; a_2 = \frac{\alpha}{2}$$

Using $\alpha = .16, K = 3$ results in the Blackman window, which reduces the first 3 sidelobes, at the expense of time resolution. However, this narrow passband makes this window ideal for convolution in the frequency domain, in which cross-frequency rejection is paramount. This phenomenon is further discussed in 2.4.

Discrete Window Width

The second consideration of windowing is the length of the window, as this determines the breadth of periodicities that are present in the windowed signal. As a rule of thumb, according to the Nyquist rate, the window width should be a minimum of 1.44 [36] times the maximal separation between sinusoids. This ensures the energy reduction of a window's first sideband will not be less than an equal-energy sinusoid. Thus, the window size N takes the form

$$N \geq 1.44 \frac{f_s}{\Delta f} \tag{2.16}$$

where f_s is sampling rate, and Δf is the minimum frequency distance. For any given case, Δf should be evaluated based on intuition and knowledge of a signal's properties. In the case of the musical example, it is fair to assume that the piano will have the largest risk of overlapping signals in the right-hand piano region, where the minimum frequency distances are well over $\Delta f \geq 20Hz$. Thus, in the case of the 10-point decimated musical recording example, $f_s = 4410Hz$, so for a $\Delta f = 20Hz$, $N = 316$ would allow for clear distinction between pitches in the DFT-transformed windowed signal. The shortcoming with large window sizes comes in computational time, as each $N - point$ window is convoluted with a portion of the signal.

However, it is unnecessary to evaluate every set of points, as a majority of the time-localized information is contained within a few standard deviations of each window. Therefore, a signal may be spaced by a window's standard deviation, rather than by

individual time-instant progression. This overcomes the computational burden, and simultaneously preserves a majority of the time-localization information.

Using these concepts, an ideal window can be designed which preserves key frequency information of its pre-windowed signal. This background is necessary to understand the STFT.

Definition

The STFT, or spectrogram, is defined as a joint time- and frequency-distribution, by performing a continuous translating convolution of a window along a signal, and taking the Fourier transform of each slice. Thus, each time-referenced window slice contains relevant frequency information. For a window $h(\tau)$, the distribution is defined thusly [4], [33]:

$$\Phi_{sp}(\omega, t) = \frac{1}{\sqrt{2\pi}} \int s(\tau) h(\tau - t) e^{-j\omega\tau} d\tau \tag{2.17}$$

Performing this operation on the downsampled musical example results in clear localization of frequency elements, in the same way that a piece of music might be written, with time shown on the x-axis, and frequency on the y-axis. The result of the STFT with a 331-point Hamming window, spaced at 104 samples/transform, is shown in Figure 2.6(a).

In this text, a red-blue heat index is used to indicate the normalized linear magnitude of a time-frequency distribution. It is read in a method similar to music, in which time lies on the x-axis and frequency lies on the y-axis. Thus, by using a rough time-alignment in Figure 2.6, the trumpet part from $500Hz$ to $700Hz$ should be immediately apparent.

While the STFT can effectively localize frequency elements, it is a one-directional distribution, in that the time and frequency energies are not preserved. These summations of energy in each domain are known as the time and frequency marginals,

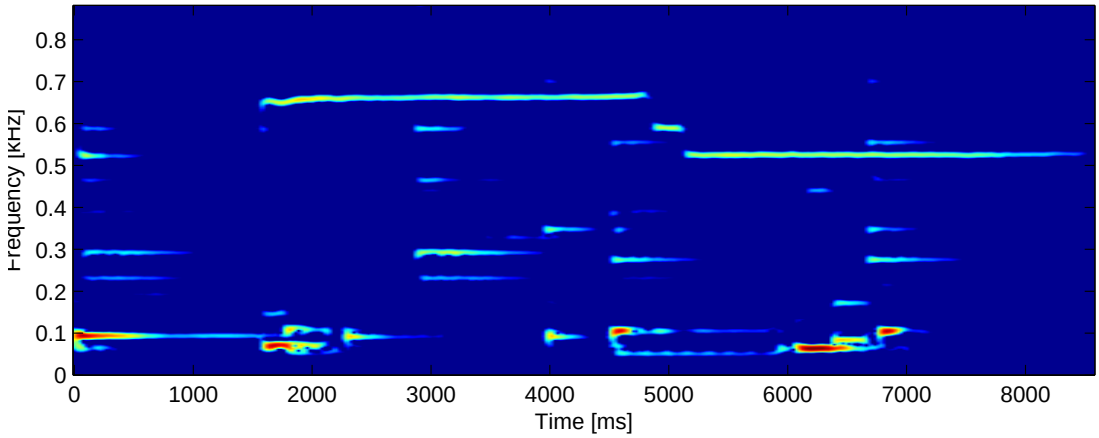

(a) STFT using 331-point Hamming window and 104-sample spacing

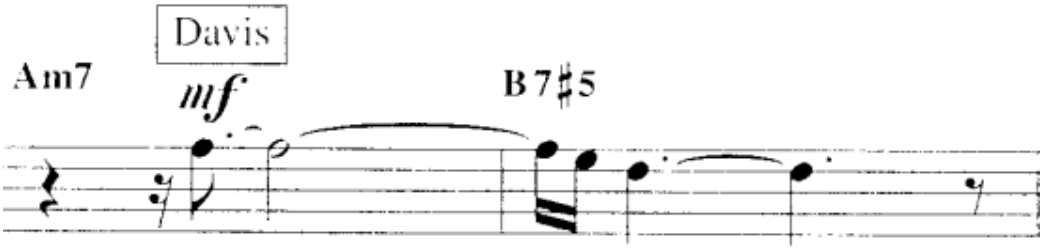

(b) Trumpet notation

Figure 2.6: Time-aligned (a) time-frequency distribution and (b) musical notation of musical example

and the STFT does not preserve these after the transformation. For this, distributions must operate on both domains simultaneously, rather than as a lossy procedure. Thus, we turn to a different class of transforms.

2.4 Cohen's Class of Time-Frequency Kernels

Wigner-Ville Distribution

The straightforward solution to the problem of the marginals is to use a signal's energy directly, such that Paseval's theorem can be exploited and retain energy equality between domains. The simplest way to do this was proposed by Ville [2], and improved upon by Wigner, in which a signal is "folded" about a time center t

and integrated along a Fourier transform. The Wigner-Ville distribution's definition is thus

$$\begin{aligned}\Phi_{WV}(t,\omega) &= \frac{1}{2\pi}\int s^*\left(t-\frac{\tau}{2}\right)s\left(t+\frac{\tau}{2}\right)e^{-j\tau\omega}d\tau \\ &= \frac{1}{2\pi}\int S^*\left(\omega-\frac{\theta}{2}\right)S\left(\omega+\frac{\theta}{2}\right)e^{-jt\theta}d\theta\end{aligned} \tag{2.18}$$

This procedure offers extreme localization to monocomponet signals. However, because this process removes the windowing convolutions, interactions between disparate frequencies create cross-term interference. In some cases, knowledge of these cross terms is useful, but for multicomponent signals, they can be detrimental to proper evaluation of spectral content. As an example, Figure 2.7 shows the Wigner-Ville distribution for the musical signal. As should be clear from visual inspection of the distribution, while the marginals are satisfied, there is extremely poor resolution within the frequency domain compared to the spectrogram. Thus, a process that uses windowing as well as preserves the information in a signal is desirable.

Generalized Definition

The solution to this problem comes in the form of windowing, but doing so in both the time and frequency domains. This can be mathematically expressed through the use of a kernel, which has the properties of a window in both domains. Thus the generalized expression for any time-frequency distribution is [4], [33]:

$$\Phi_C(t,\omega) = \frac{1}{4\pi^2}\iiint s^*\left(u-\frac{\tau}{2}\right)s\left(u+\frac{\tau}{2}\right)\phi(\theta,\tau)e^{-j\theta t-j\tau\omega-j\theta u}du\,d\tau\,d\theta \tag{2.19}$$

where the kernel, $\phi(\theta,\tau)$ serves to reduce interference between cross terms. For example, setting $\phi(\theta,\tau)=1$ results in the Wigner-Ville distribution, which offers no cross-term protection. Several key time-frequency distributions use intuitive substitutes for the kernel to reduce the cross-term interference. The Choi-Williams distribution, for example, uses a Gaussian kernel of $\phi(\theta,\tau) = e^{-\theta^2\tau^2/\sigma}$, where σ may

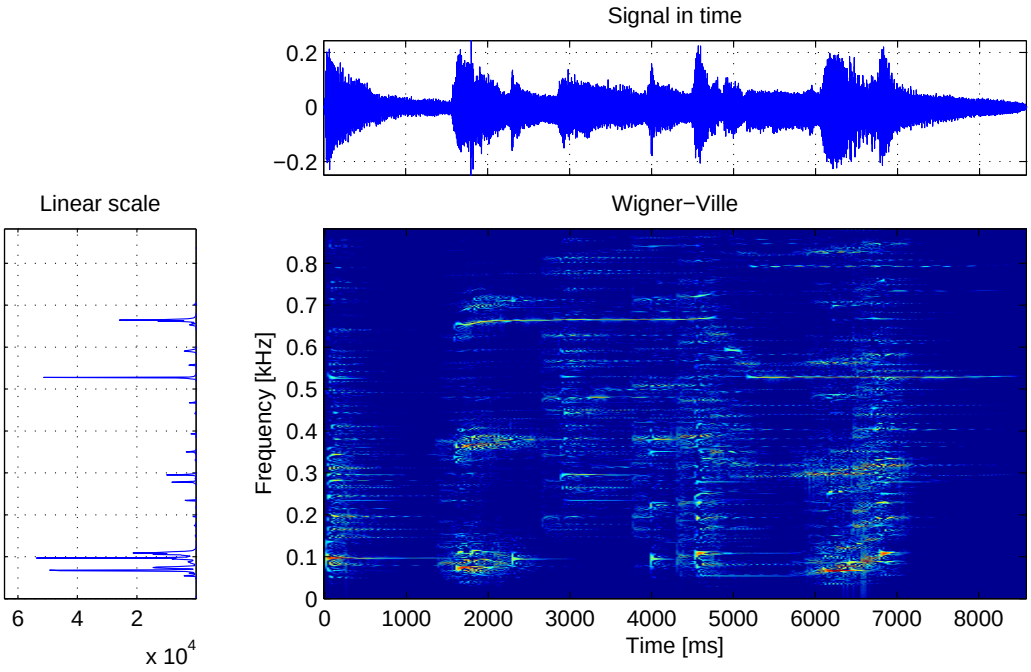

Figure 2.7: Wigner-Ville distribution with spectrum and time domain signal displayed alongside time- and frequency-aligned axes for musical example

be tuned as per the needs of the distribution. This results in a satisfaction of the marginal energy conservation, while reducing cross-term interference.

A closely related distribution, the reduced interference kernel, uses the qualities of the Hann window to smooth the interference. It is known as the Hann window reduced interference distribution (RID), and its equation is given by

$$\Phi_{RID}(t,\omega) = \int_{-\infty}^{+\infty} h(\tau)\, R_x(t,\tau)\, e^{-j2\pi\nu\tau}\; d\tau, \tag{2.20}$$

with

$$R_x(t,\tau) = \int_{-\frac{|\tau|}{2}}^{+\frac{|\tau|}{2}} \frac{g(v)}{|\tau|} \left(1+\cos(\frac{2\pi v}{\tau})\right)\; x(t+v+\frac{\tau}{2})\; x^*(t+v-\frac{\tau}{2})\, dv$$

The Hann Kernel can be clearly seen, in the integration of the autocorrelation function, and the overall function can be considered a smoothed Wigner-Ville distribution. Thus, the distribution is adept at reducing interference between cross terms. Figure 2.8 shows the distribution of the musical example, with extremely clear localization of each note and noticibly less interference when compared to the WV

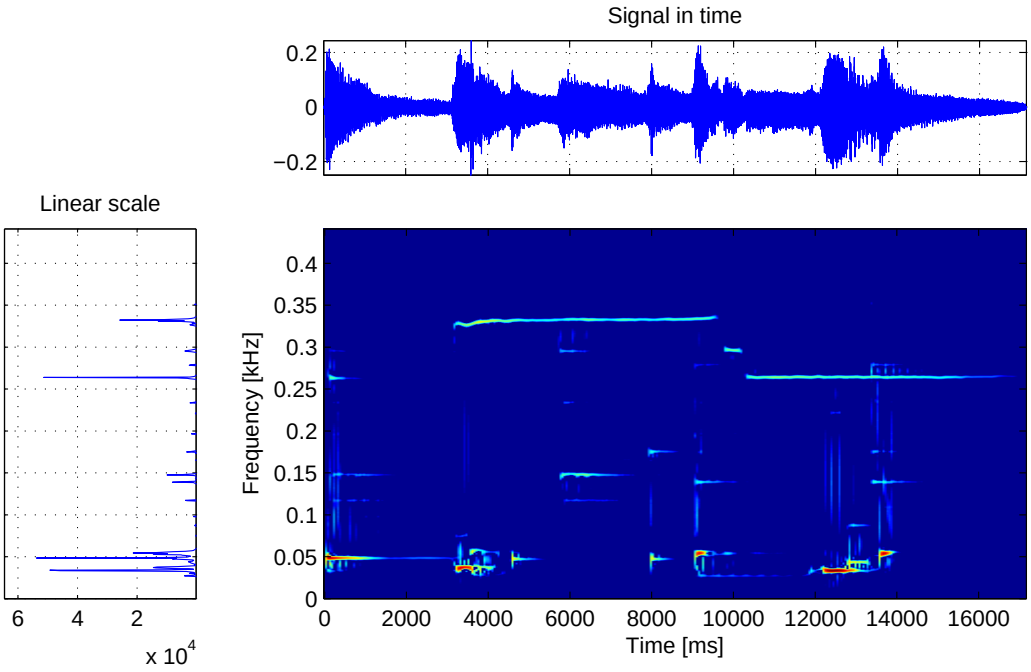

Figure 2.8: Hann Window RID with spectrum and time domain signal displayed alongside time- and frequency-aligned axes for musical example

distribution of Figure 2.7. Using this kernel, a distribution which both satisfies the marginals and accurately time-localizes may be obtained. By satisfying the marginal properties, the time-frequency transform may be integrated along specific times and frequencies and reliably represent the content along that range. Thus, even in the case of a complex multicomponent signal, the RIDH kernel effectively separates and evaluates the time-localized spectral content. For these reasons, this kernel will be used when analyzing the multicomponent signals generated by surface electromyography.

2.5 Summary

This section examined several key concepts necessary to evaluate non-stationary signals. It was first shown that the Fourier transform, when coupled with statistical analysis techniques, could provide useful high-level insight into signals. However, when dealing with non-stationary signals, several additional considerations had to be

made.

The use of windowing helped fix problems caused by using a rectangular cutoff, while the use of the analytic signal circumvented problems of the Fourier transform's symmetric nature. This discussion gave way to an explanation of cross-term distortion, and finalized the usefulness of the Hann-windowed reduced interference kernel, which represents a straightforward tool for analyzing the changing frequency content of non-stationary signals. Section 4.5 will pick up this discussion in the context of sEMG signals, after a discussion in Chapter 3 of the qualities of sEMG signals and their interpretation in the context of gait.

Chapter 3

Physiology

In Chapter 2, the critical need for signal knowledge was made apparent. The selection of the window, window size, and kernel type are tied to the accuracy of the time-frequency analysis. In this chapter, the physiology of both gait and surface electromyography (sEMG) signals will be examined in detail, in order to properly constrain the signal analysis.

First, a general discussion of human neuromuscular activation will be discussed in section 3.1, which will be extended to sEMG signals. This will be further developed with a discussion of the interpretation of sEMG signals 3.3 in the context of time-frequency analysis. Next, a background discussion of human physiology changes during gait will be discussed, as well as relevant literature dealing with the changes observed in gait patterns under certain neuromuscular conditions in section 3.4. This is extended to discuss the gait-sine algorithm in the next chapter, section 4.2, which was developed to extract gait information using a pressure-sensitive mat of chapter 4.

3.1 Muscular Model

The human body's methodology for signaling muscular contraction allows for evaluation of the electrical impact of the neuromuscular systems. When the brain deems contraction necessary, a small electrical signal is sent along the nervous system to the relevant area of the body. These nerve axons attach to groups of individual

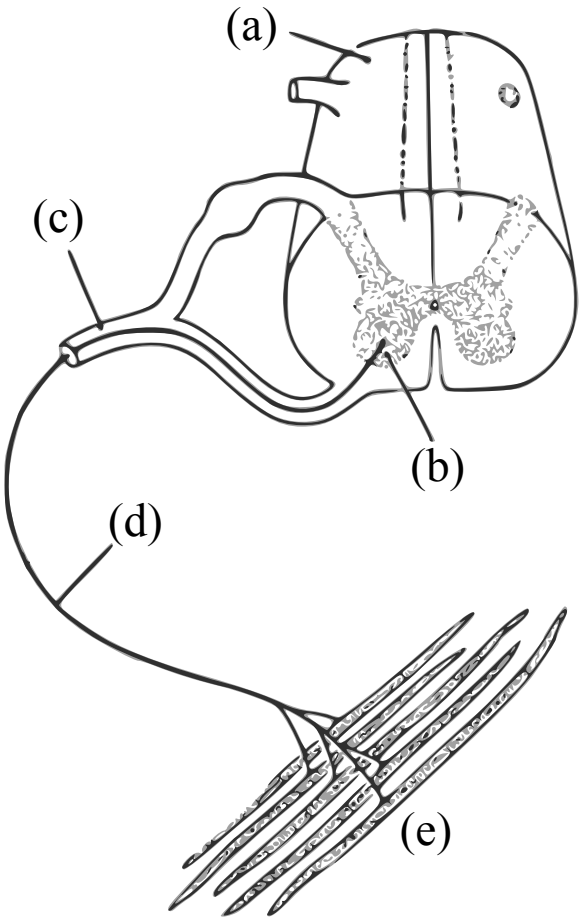

Figure 3.1: Diagram of muscle signaling from (a) spinal cord, (b) neuron cell body (c) spinal nerve, (d) nerve fiber, and (e) termination at muscle fiber [10]

muscle fibers known as *motor units*. As the nervous system fires its electrical impulses, individual fibers contract at a rate proportional to the rate of firing. This arrangement of signaling, from the spinal cord neuron to the muscle fibers themselves is shown in Figure 3.1, adapted from the Basmajian text [10].

Thus, a motor unit can be considered as groups of impulse trains corresponding to individual muscle fibers, and with a frequency which varies with contraction speed. The number of muscle fibers activated within each unit varies widely, but corresponds to the specificity of moment required. Thus, precision units such as the eye have much fewer fibers per neuron, while limbs and flexors coarsely control larger fiber sets.

The composite nature of muscle fibers within multiple motor units result in var-

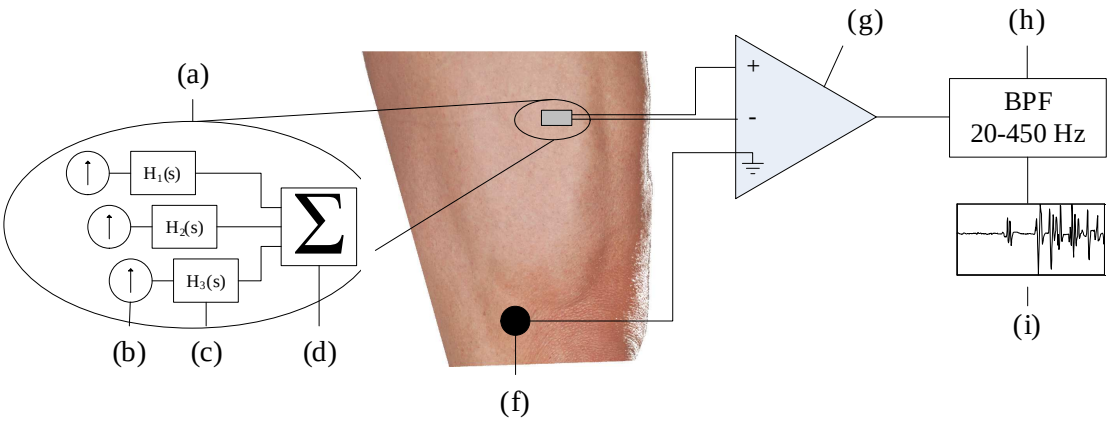

Figure 3.2: Diagram for sEMG signal acquisition, with (a) expanded system-level interpretation of muscle firing summation with (b) individual motor unit firings, (c) varied subcutaneous filters, and (d) summation at skin surface; Acquisition by (e) sEMG sensors with (f) electrical distant ground feeding (g) differential amplifier, (h) filtered using band-pass rejection results in (i) final sEMG signal

ied firings under the skin surface. These varied locations emanate electrical signals through the skin, which operates as a generally low-pass filter, are then shaped by varying degrees over the length of the subcutaneous layers of muscle, fatty tissue, and skin. The result at the surface is then a composite of distinct and overlapping motor unit firings. This summation is known as a motor unit action potential (MUAP), and is the primary focus of sEMG.

3.2 Surface EMG Measurement

In order to understand the translation from motoneuron activation to final sEMG signal, Figure 3.2 shows an expanded diagram of each stage of the signal from start to finish. As previously discussed, a set of motor units (a) is the result of the summation of multiple impulse trains (b) propagated through varied filters (c) corresponding to varied distances from the skin surface (d) and layers of subcutaneous tissue.

At the skin surface, a dipole electrode (e) is tied to a differential amplifier (g) with an electrically distant ground (f) for acquisition. Differential amplification is used to

reject common-mode signals, such as 60-cycle hum or other interference, while the skin serves as a voltage reference to reject electrical currents traveling within it. Finally, as a majority of neuromuscular activity is in the 20-450 Hz bands, the signal is band-pass filtered (h), resulting in the final signal (i).

The resulting signal is thus the composite, filtered summation of the motor units nearby. Muscle fiber firings lose electrical strength at a rapid pace, so the location of the sensor is of primary importance [10]. The exact specifications of the sEMG sensors used is described in section 4.1. Thus, there are many factors at play when interpreting sEMG signals.

3.3 Surface EMG Signal Interpretation

When considering precisely how to interpret the final sEMG signal, several considerations should be taken into account. From section 3.1, it should be clear that a sEMG signal is not representative of a single muscle fiber, but is the result of the summation of disparate firing fibers contained within a single muscle. Thus, considering a signal, the final result should be thought of as a composite of varying amplitudes and frequencies. Based on this model [10], several assumptions can thus be made

- Signal amplitude is proportional to the number of simultaneous firings occurring in a motor unit group
- Signal amplitude is dependent on the radius of the muscle fiber
- Individual firings reaching the skin surface at disparate times will increase the perceived frequency
- Individual pulsations will affect the spectrum shape around
- High-frequency filtering occurs due to subcutaneous tissue and distance

These findings are combined into a model of the power spectrum, which can be used to evaluate isometric contractions.

Spectral Analysis

There are several considerations when evaluating the spectrum of a continuous isometric contraction. However, the use of time-frequency analysis bypasses these problematic effects. Thus, time-frequency analysis can be used to evaluate time-dependent fiber activations rather than examining the composite power density spectrum.

However, past investigations of the power density spectrum during contractions gives additional insight into the interpretation of the time-localized signals. A summary of the relationship between signal amplitude and frequency as a function of force (F) and time (t) is shown in Figure 3.3. This figure is adapted from the composite of several authors' findings [10], [37]. The function follows a modified Bessel function of the second kind, and is dependent on time, force, and frequency. Its shape is due to the effect of the subcutaneous tissue and distance on the sEMG sensor, which affect the spectrum in a predictable manner.

Considering the graph, there are several key elements that should be considered when evaluating any spectrum generate by a sEMG signal. First, the largest concentration of energy lies between 60 and 120 Hz, and shifts in magnitude with force. It also shifts lower in frequency as time progresses during a sustained contraction. Thus, initial motor unit recruitment will produce energy in the 80 Hz range, and over time shift towards 40 Hz. Additionally, a spike is clear between 10-40 Hz. This is interpreted as low-frequency motor unit firing. As force (and motor unit recruitment by extension) increase, these low-frequency firings are subsumed by the main lobe at 80 Hz. A second notch occurs at 160 Hz, though this notch can range from 100-200 Hz, and is reflective of the conduction velocity of the nerve fibers. In the initial stage of a contraction, the lower number of recruited motor units reflect much higher perceived

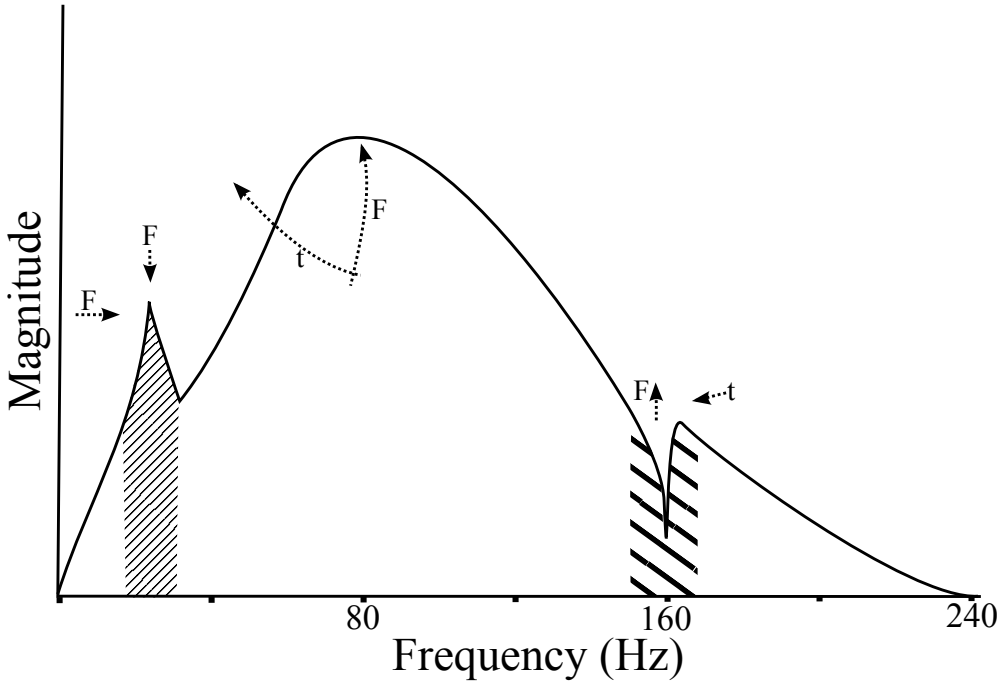

Figure 3.3: Graph of relevant force and temporal effects on power density spectrum

velocities, and thus higher frequency. As the contraction sustains, the conduction becomes indistinguishable, and is again subsumed towards 80-100 Hz. Thus, energy can be measured, especially using time-frequency analysis, by investigating these key frequency elements.

Age and Gender

In addition to the overarching implications of the frequency content of sEMG signals, some consideration should be given to relevant differences in age and gender. The phenomenon of sarcopenia, which begins around the fifth decade, refers to the loss of muscle fiber, and therefore contraction force. This results in a slightly larger number of recruitment to achieve the same level of force [38], [39]. Thus, older individuals may have slightly varied neuromuscular compositions when compared to young.

However, at higher levels of force, the differences in the sEMG signal become less prevalent, especially at the point at which the low- and high- frequency analomolies shown in Figure 3.3 are subsumed by the medium frequency [37], [40]. Thus, in the case of analysis of muscles associated with ambulation, it is safe to assume that the normalized energy from 40-120 Hz will be comparable between young and old populations. Chapter 4 will discuss the use of metrics to exploit this fact.

Additionally, several relevant gender factors should be considered when examining the spectral distribution of sEMG signals. First, it is well known [41] that the subcutaneous fat and concentration thereof is higher in females compared to males. Additionally, the metabolization rate of fat is loweer compared to males [42]. As explained previously, subcutaneous tissue acts as a low-pass filter, resulting in a lower concentration of mean frequency during contraction. Therefore, when evaluating any frequency-based analysis between male and female subgroups, it should be expected that a male group will give slightly better resolution than a female group.

This fact is augmented by the overall higher amount of lean muscle in males than that of females [43]. However, these differences surprisingly do not result in highly disparate motor unit recruitment or firing patterns [44]. These factors combine to manifest in differences at the point of contact for sEMG measurement between males and females. Due to the experimental design, which favors minimal intrusion, needle-point EMG was not used, and therefore these key physiological differences manifest as quantifiable differences between the genders.

Finally, females show higher levels of activation in the tibialis anterior muscle [45], most probably due to cultural impositions on footwear norms in males and females. Additionally, anatomical variations translate to gender-dependent ambulation patterns [46], which creates additional disparity between gendered sets. Thus, when evaluating discrepancies in sEMG signals on specific muscles, there may be some variability in accuracy between muscles when comparing the genders as well. These

gender differences are made apparent in the context of the research in sections 5.2 and 5.3, with additional discussion in section 5.4.

3.4 Gait

Human locomotion is not a simple thing. There are multiple variables at play when any fully-developed adult walks, including spatial awareness, muscular contraction, and evaluation of forces necessary for locomotion [47]. Thus, because of its complexity, gait abnormalities can manifest from a myriad of causes, including neurological, muscular, or confounding comorbidities that may increase the difficulty of specific diagnoses [48]. However, after identification of the cause of gait abnormality, a subject can be adequately treated.

As discussed in chapter 1, falls are the primary cause of death in senior adults, and therefore falls and fall risk factors serve as an area of prime investigative need. One key condition that is highly common in seniors is that of hypertension. It has also been shown [31] that hypertension can affect gait, though this relationship is difficult to quantify, especially compared to other common gait dysfunctions which may be much more obvious [48], such as Parkinson's or other primarily neurological conditions. Hypertension, however, is a vascular condition, which may underscore its effects on gait degradation [49].

Thus, an investigation into the correlation between hypertension and gait represents a notable area for evaluation. For this to occur, a key first step must be made in evaluating the gait cycle to deliver consistent quantitative results. For the analysis of gait, there exist several methodologies that have been around for some time to separate portions of the gait cycle from one another. Through the use of time-based visual inspection [50], accelerometers, pressure devices [51], or kinematics [52], gait cycles have been assessed with a measure of quantifiable reliability.

However, kinematics-based methods require additional equipment for measurement of gait information when compared to inspection-based methods, especially wearable sensors or light-reflection points for measurement. Pressure-based systems provide equal performance to classical visual inspection methods [51], with much-reduced interference to the normal walking pattern. There is little work done in comparison of the observer effect these sensors have on subjects under study, but it stands to reason that minimizing the impact of sensors should always be considered. As this experimental setup seeks to examine muscular response using sEMG sensors, as described in chapter 4, kinematics could prove difficult. Thus, a pressure-sensor approach is used, which can then exploit the natural gait cycle for isolation of relevant portions. This will be further explained in the context of the experimental setup in the next chapter.

3.5 Muscle Selection

Through the course of a single gait cycle, there exist several key sections during which a variety of muscle groups activate. In order to evaluate the state of each muscle during gait, some considerations for muscular activation should be made in the context of the gait cycle. First, those muscles which offer a low skin-impedance level should be considered. Next, practicality for the experiment presents a key consideration. Finally, representation of the entire gait cycle [47] should be considered.

For reference, Figure 3.4 shows the location of each of the four primary muscles used in the experimental setup. Figure 3.5 shows these same muscles' normalized sEMG signal for an averaged selection of gait. In both figures, the muscles are ordered as (a) vastus lateralis, (b) tibialis anterior(c) biceps femoris, (d) gastrocnemius. These muscles will each be briefly discussed in the following sections.

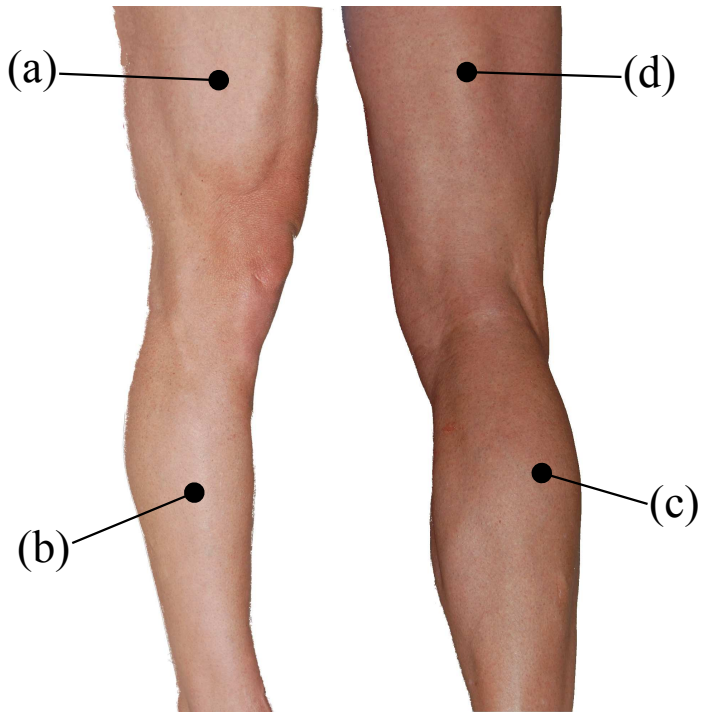

Figure 3.4: Leg muscle diagram indicating location of (a) vastus lateralis, (b) tibialis anterior, (c) gastrocnemius, and (d) biceps femoris muscles

Candidate Muscles for Measurement

Vastus Lateralis

In the quadriceps group, the vastus lateralis represents both the largest and strongest muscle of the four. It is used primarily during the loading phase, as it is necessary to maintain the leg rigidity through the swing, as can be seen in Figure 3.5 (a). Because of its size, the vastus lateralis has a much lower skin impedance, thus increasing the signal availability using sEMG sensors.

The vastus lateralis is located on the front outside of the leg, as shown in Figure 3.4 (a), making it easily accessible for sEMG measurement. In addition to low impedance, because it is the largest muscle in the quadriceps group, it provides a much larger number of muscle fibers activating at a given point. Thus, because of its singular activation and accessibility, the vastus lateralis represents a good candidate

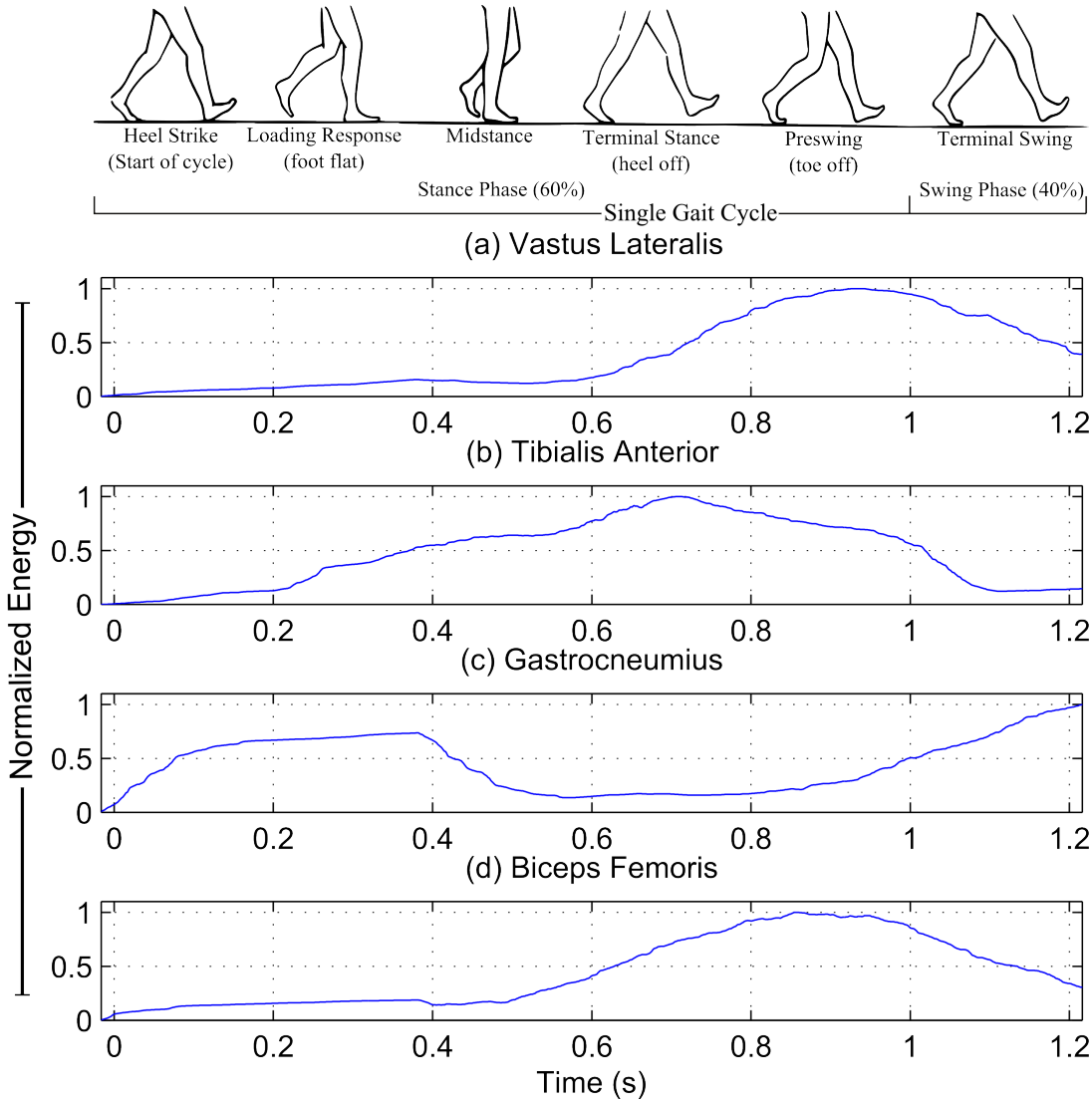

Figure 3.5: Gait cycle aligned with normalized EMG voltages of (a) vastus lateralis, (b) tibialis anterior, (c) gastrocnemius, and (d) biceps femoris muscles

for analysis of sEMG signal during the gait cycle.

Tibialis Anterior

The tibialis anterior lies on the outside of the shin, as seen in Figure 3.4 (b), and is responsible for dorsiflexion and plantar flexion of the foot. This translates to usage during loading and push off phases, in which dorsiflection is necessary to receive the surface, and plantar flexion executes the extension of the energy through the

foot to the surface. Thus, there are two periods of innervation that often seamlessly transition through the stance phase of the gait cycle. This seamlessness can be seen from Figure 3.5 (b), with some indication of two key points at time $t = .4s$ and $t = .7s$.

Additionally, the tibialis is a fairly large and low-fat muscle, making it easy to access and minimizing the chance for interference from other muscle groups. Due to this key period of time lengthening, the tibialis is a good candidate for sEMG analysis.

Gastrocnemius

The gastrocnemius muscle is the chief calf muscle, shown in 3.4 (c). It is connected to the ankle, and is thus used in opposition to the tibialis anterior during the swing phase and during loading. Due to these two separate activations, it was necessary to isolate one using the gait-sine algorithm, which is explained in section 4.2. In addition, this double-activation can be seen in Figure 3.5 (c).

The simplicity and the use of the gastrocnemius were exploited in the initial investigation of the gait cycle [53], as the heel strike impact point to toe-off could be used as a rough estimate of the gait-window for activation of this muscle. These findings were definitive and were expanded in the current work, and was straightforward to calculate.

In addition to its accessibility and comparative size, the gastrocnemius represents a key area of the gait cycle in which few other muscles are operating. Because it is the largest muscle in the calf group, it makes a prime candidate for examination.

Biceps Femoris

The final muscle group is that of the biceps femoris. This muscle belongs to the hamstring group, and sits on the outside of the group and is responsible for knee

flexion, as shown in Figure 3.4 (d). This muscle is slightly less accessible than other muscle groups, but represents a second muscle group which indicates knee flexion, as with the vastus lateralis.

As can be seen in Figure 3.5 (d), the normalized activation is similar to that of the vastus lateralis; during the swing phase, it is necessary for both muscle groups to activate in order to keep the shin in alignment. However, the vastus lateralis is used again later during loading, while the biceps femoris are not.

Of the muscles selected, the biceps femoris represented a much smaller number of muscle fibers in the motor unit. These factors, combined with occasional difficulty with adhesives, translated to lowered usefulness in detecting discrepancy in the experimental stages. This fact becomes apparent in sections 5.2 and 5.3.

Non-Candidate Muscles

Due to the limitations of the sEMG acquisition apparatus, only four muscles could be individually measured. It is for this reason that the above four muscles were selected. The selected muscles represent the key areas of the gait cycle, and in many cases were also the largest muscles in their respective groups. However, there are two muscle groups which were not represented, yet are pivotal for gait. These are given consideration below.

Pelvic muscles

The muscles surrounding the pelvis, comprised of the gluteus maximus, minimus, and medius, represent another key muscle group for locomotion. These activate during the swing phase to propel the leg backwards, and thus the body forwards. Though gluteus maximus is the largest muscle in this group, its size causes significant difficulty for obtaining consistent sEMG signals, as it stretches around the pelvis, making consistent location difficult. Additionally, sEMG sensor placement requires access to

this culturally taboo location, further exacerbating the problem. Additionally, the portion of the gait cycle in which this muscle activates is paralleled by the activation of the biceps femoris, thus rendering its coverage unnecessary.

Abductor Group

In addition to the gluteus muscle group, the abductor hallucis and abductor digiti minimi represent muscles responsible for plantar flexion of the toes. Although the use of the toes is extremely important for balance (and therefore gait), they are highly inaccessible for sEMG analysis during gait.

3.6 Summary

This chapter examined several key physiological factors for consideration when evaluating surface EMG signals. First, the basic neuromuscular system of human muscle was explained, specifically in the context of the complexities of muscle innervation. The corresponding sEMG interpretation of these signals was discussed next, the key takeaway of which should be the force-frequency relationship centering on the 40-120 Hz band. As motor unit recruitment increases, the sEMG amplitude at this frequency also increases, while low-activation signaling at both lower and higher frequencies will be subsumed by this band.

Following the discussion of sEMG signals was a brief discussion on human gait, specifically the trade offs of various methods for gait cycle acquisition and analysis. This discussion will be continued in section 4.2, which discusses selection of sEMG signal slices in the context of the gait cycle. Finally, consideration was given to the methodology behind muscle selection, resulting in the finalization of four key muscles from various muscle groups responsible for gait. The background information from the previous two chapters will be combined in hapter 4, which will discuss the

experimental setup and application of time-frequency analysis to the relevant sEMG signals.

Chapter 4

Experimental

Having discussed the relevant background for the evaluation of hypertension using sEMG and gait information, it is necessary to develop an experimental setup that can acquire and interpret this information. This chapter will begin with an explanation of the experimental setup used in section 4.1, including a detailed explanation of the apparatus used to acquire the information, as well as relevant medical information gathered. Next, section 4.2 discusses the use of the gait-sine algorithm, which is designed to take advantage of the sinusoidal properties of gait for signal separation. Section 4.3 discusses the state of the subject database in the context of the subjects with varying conditions, as well as the justification for mixing subsets for analysis. Section 4.4 will discuss the pre-treatment of the subject database sEMG signals, especially the procedure for subject exclusion based on data acquisition. Finally, sections 4.5 and 4.6 will discuss the application of time-frequency analysis to the gait-separated signals and the use of metrics based on section 3.3's discussion of sEMG interpretation.

4.1 Data Acquisition and Setup

To compare a large number of subjects, and to ensure statistical robustness, an experimental setup which simultaneously records gait and sEMG information is necessary. As previously discussed in section 3.4, kinematic-based gait assessment adds bulk to the subject, and when used in conjunction with sEMG sensors, the clutter

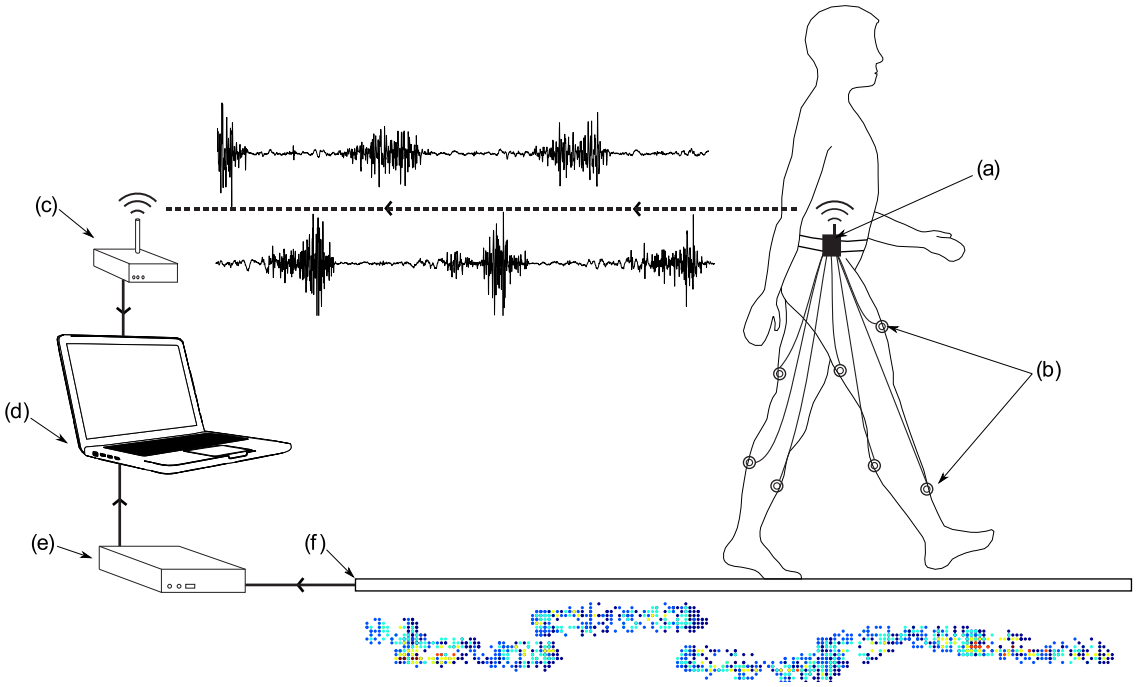

Figure 4.1: Diagram for experimental setup with (a) belt-worn sEMG transmitter unit, (b) sEMG sensors connected to muscles, (c) wi-fi receiver with example sEMG signal, (d) data recording computer, (e) walkway data converter, (f) pressure-sensitive walkway with example footfall pressure signal

would render the experiment impractical. Thus, a pressure-sensitive mat is used. Additionally, as sEMG sensors must record during ambulation over a long distance, a wireless sensor apparatus is used. These two devices are tied together using a trigger mechanism designed as a latch, such that at the start of acquisition from the sEMG device, a pulse is sent to the mat.

In order to visualize this setup, Figure 4.1 shows the apparatus, complete with the diagram of a test subject under the full experimental setup. The wireless sEMG system (b) used was a Delsys Myomonitor 8-channel dipole-electrode system. The signals are transmitted using Wi-fi (a) to a host computer (c) receiver (d). The pack (a) has a $1kHz$ sampling rate, as well as a bandpass filter between $20 - 450Hz$ for noise and dc-level rejection. These frequencies contain the majority of sEMG signal information, and are beneficial in rejecting both ambient and high-frequency noise [54].

The sEMG sensors use a dipole-electrode configuration, as described in section 3.2. The sEMG acquisition system uses two $1cm$ long silver-plated contacts spaced $1cm$ apart attached using an adhesive. These are sized to reject cross-talk interference from the muscle measurements [55]. These elctrodes are tied to a differential amplifier, as in Figure 3.2. The amplifiers and reference voltage used achieve a CMRR of $-92dB$ with an ambient noise RMS level of $1.2\mu V$ [56]. Thus, several steps are taken to obtain the sEMG signal alone.

Meanwhile, gait information is obtained using the pressure-sensitve GaitRITE mat (f), which is a 1m $\times$ 6m long runway with 48$\times$384 3-bit pressure sensors. The GaitRITE was used due to its fidelity towards extant gait measurement methods [51], as well as its built-in trigger synchronization and direct data export features. The mat is connected to a separate recording unit (e) that polls with a 60-Hz sampling rate, sending data to the host computer (d), concurrent with sEMG acquisition. This sampling records footfall pressure changes in time over the length of the mat. The trigger (not shown) is a NI digital IO board that releases a $1\mu s$ pulse upon sEMG recording. This pulse feeds to a $1ms$ Schmidt trigger, whose output is tied to the mat recording unit (e), which registers the $1ms$ pulse as a non-pressure event. The Schmidt trigger is necessary to ensure that a "high" value during one 60-Hz sampling cycle, and thus is recorded as a non-pressure event in the raw data export from the mat recording.

All data is exported to .CSV format, where it is imported into MATLAB for analysis. Data from the mat is upsampled at a ratio of ${}^{1000}/_{60} = 16.67$ with data interpolation performed by an averaging filter and time aligned to the sEMG data using the trigger-point generated by the sEMG acquisition software. Data before and after the first footfall pressure point is truncated, and the remaining data is evaluated according to the processes described by sections 4.2, 4.4, and 4.5.

In order to make adequate assessments of differences between populations, sub-

ject selection was not limited by age, gender, ethnicity, or disease. Subjects include ambulatory individuals who can walk with or without assistive devices. Subjects' mental status was evaluated using the Folstein Mini-Mental Exam [57] (MMSE), and participants who scored below 25 were not included in results examination. Subjects answered a self-report survey on medical history, which were corroborated by subjects' medical history for those over age 65. Subjects were asked to complete these steps prior to undertaking the experiment, and were subject to informed consent prior to the experiment.

Prior to participation, subjects were provided with optional gym shorts to facilitate ease of sEMG sensor application. After this, dipole sEMGs along the direction of muscular activation in the muscle groups described previously in section 3.5: the tibialis anterior, the gastrocnemius, the vastus lateralis, and biceps femoris. Subjects performed two pairs of walks for recording at self-selected speeds. The first pair was self-selected as "Normal pace," while the second pair was "fast-paced," using verbal cues to describe these two speeds. Acceleration and deceleration lines were prepared at 2m before and after the pressure-sensitive mat in order to minimize variability during the walk recordings.

4.2 Footfall Separation by Gait-Sine Algorithm

The gait pattern involves a gradual, slow, sinusoidal shift of the center of mass during ambulation [47]. This is visualized in Figure 4.2 by considering the leminscate (c) shown. As the lateral (a) center of mass corresponds with the center of pressure seen by the mat, a sine wave can be interpolated using the pressure recorded on the mat in varying levels. The pressure concentration at a given point gives a good estimate for the center of mass, and using the this information from the mat, an estimate of the center of mass is straightforward. The sine wave can then be used to

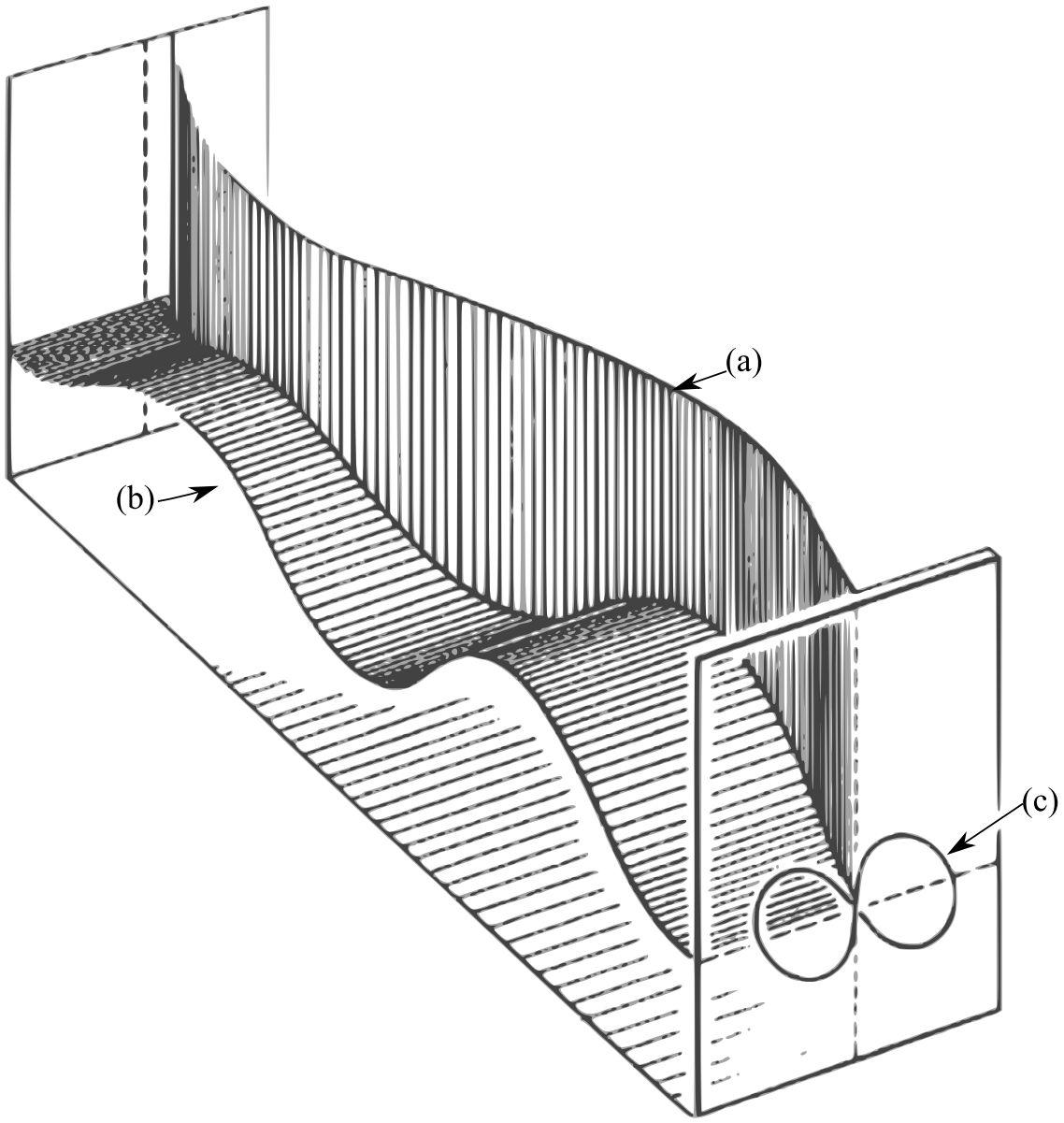

Figure 4.2: 3-dimensional graph of center of mass during gait, with (a) lateral and (b) vertical directions with (c) lemniscate pattern shown; image adapted from [47]

isolate and estimate gait.

In order to go from the mat information to a sine wave, an intuitive algorithm is used. First, the algorithm uses the mean pressure point for the walk as a division for left and right footfalls. Then, each first time moment is calculated using pressure information for each footfall, either left or right. These pressure time-moments serve to give an estimate of the pressure center at a given time. Finally, these moments

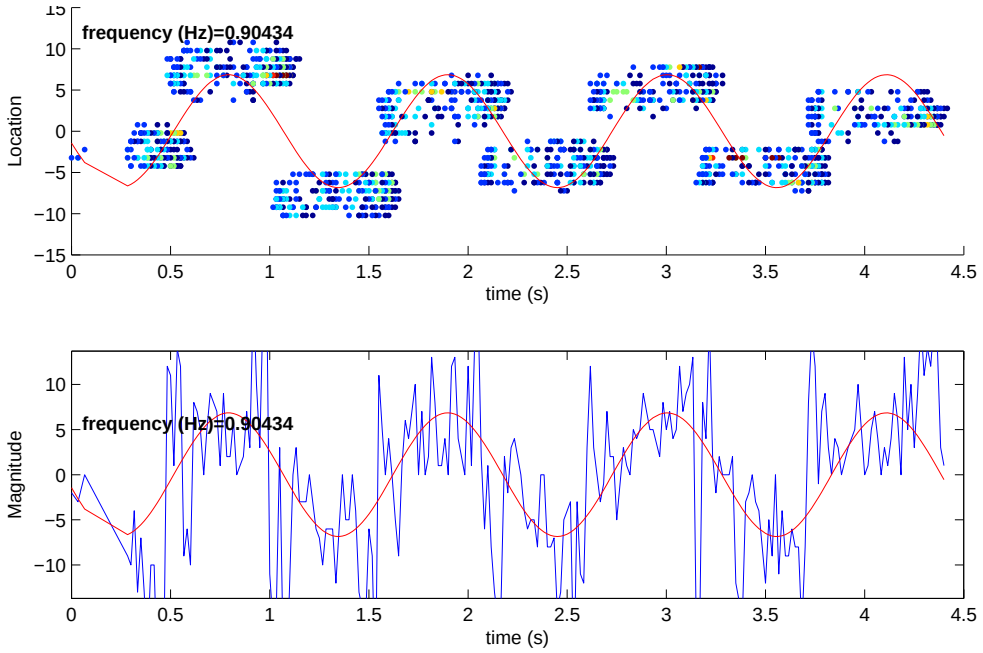

Figure 4.3: Walk recording of subject 015 with pressure summation and superimposed best fit sinusoid shown

are used to generate a pressure map, which is then fit to a sine wave using a least-squares routine. The result of this maps a sine wave to each footfall. Figure 4.3 shows this process, with the top portion showing pressure recording, and the bottom portion showing the pressure-moment calculations. The least-squares sine wave is superimposed on both figures, and clearly corresponds to the gait cycle in the top portion of the figure.

The peak periods of muscular activation during ambulation have been known for some time [58], which consequently exhibit measurable activity in the neuromuscular systems controlling the gait. Thus, they are prime candidates for sEMG recording. The benefit of using the gait-sine algorithm lies in its consistency from subject to subject, as all ambulatory individuals will follow a sinusoidal center of mass over the course of their gait cycle. A visual example of this is shown by Figure 4.4, which includes typical normalized energy for normal gait. This figure is he same as Figure 3.5 of the previous chapter, and is repeated for clarity. Table 4.1 contextualizes this

knowledge by the gait-sine algorithm, with the gait cycle portions mapped to the center of mass sine wave phases, as well as the verbal descriptors of these gait cycle portions. Thus, sEMG signals are selected over the principal period of activation according to the relevant portion of the gait cycle.

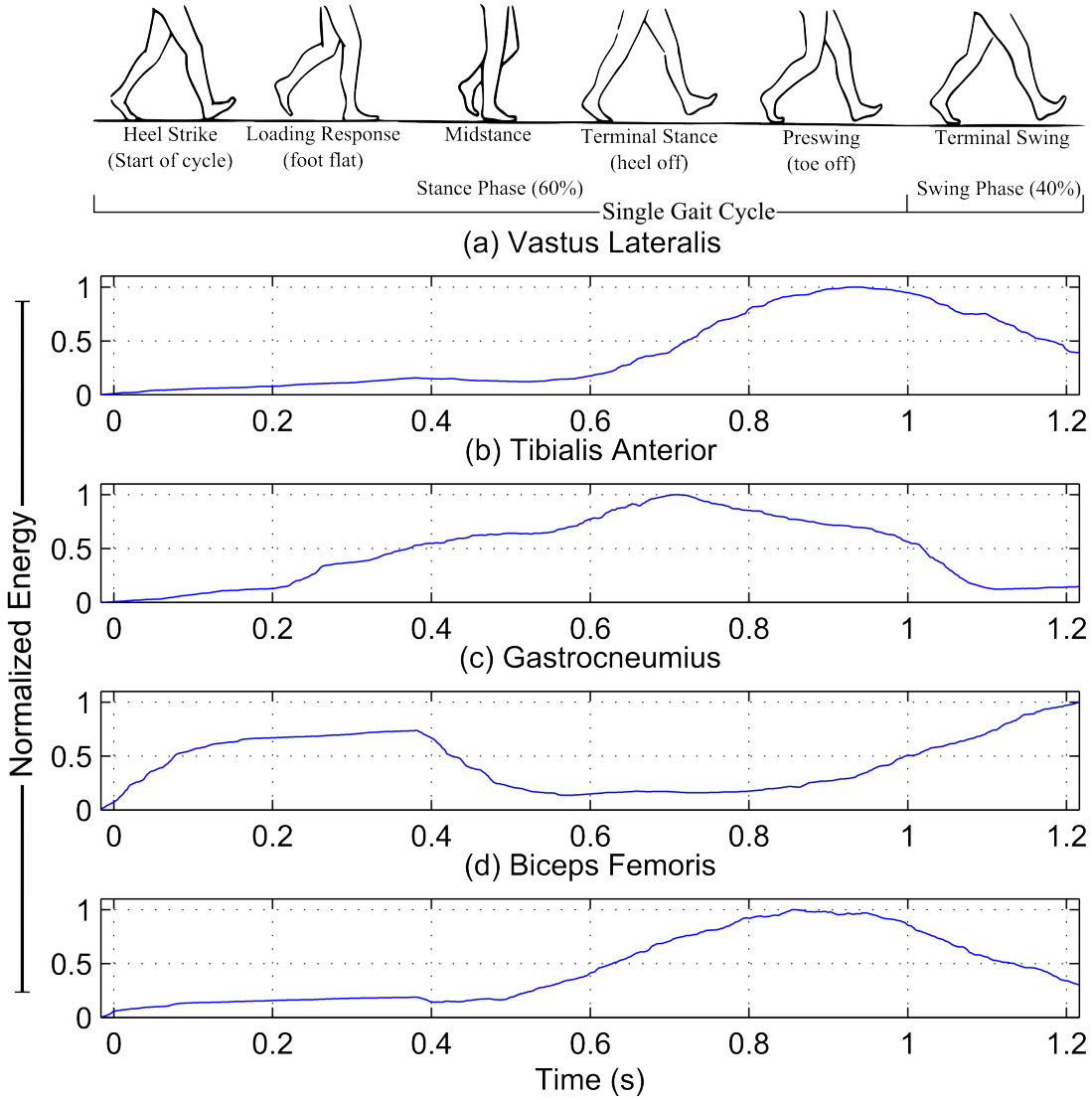

Figure 4.4: (Repetition of Figure 3.5) Gait cycle aligned with normalized EMG voltages of (a) vastus lateralis, (b) tibialis anterior, (c) gastrocnemius, and (d) biceps femoris muscles

Figure 4.5 shows a composite recording of the left and right tibialis anterior muscles, with time-aligned footfall pressure information. This figure is representative of

Table 4.1: Gait cycle activation by muscle with appropriate gait-sine parallel

Muscle Name	Cycle (%)	Phase Range	Gait Portion
Tibialis Anterior	$25\% - 62.5\%$	$\pi/2 - 5\pi/4$	Midstance to toe off
Gastrocnemius	$0\% - 66.7\%$	$0 - 4\pi/3$	Heel strike to toe off
Vastus Lateralis	$32.5\% - 62.5\%$	$\pi/3 - 5\pi/4$	Midstance to heel off
Biceps Femoris	$32.5\% - 62.5\%$	$\pi/3 - 5\pi/4$	Midstance to heel off

a single walk of the four-walk set, with two of the eight recorded sEMG signals. In addition, the gait-sine pressure fit is superimposed on the figure, with the estimated sEMG signal divisions shown based on the algorithm. Also clear in the figure, bars at $\pi/2 - 5\pi/4$ correspond to the optimal activation of the tibialis anterior, whose left and right sEMG signals for that subject are shown, which are those points indicated by Table 4.1 as the periods of peak activation. Thus, using the gait-sine algorithm, a consistent window for sEMG activation intervals can be extracted. Furthermore, when comparing person-to-person muscular activation, this gait-cycle selection serves to compare the same portion of the gait cycle, regardless of walking speed or other conflating factors. This allows for comparison between disparate subject groups and eliminates conflating factors.

4.3 Database Subsets

For accurate diagnosis of the presence of hypertension, data must be divided into relevant subsets, in order to tease out conflating factors that may be present. Thus, the subjects are subdivided over a wide set of criteria. First, it is assumed that the lack of significant changes in motor unit action potential due to aging [37] allows for the inclusion of both senior subjects and young subjects in the control set. This is offset by the decline in the number of motor units overall after age 60 [59], as was

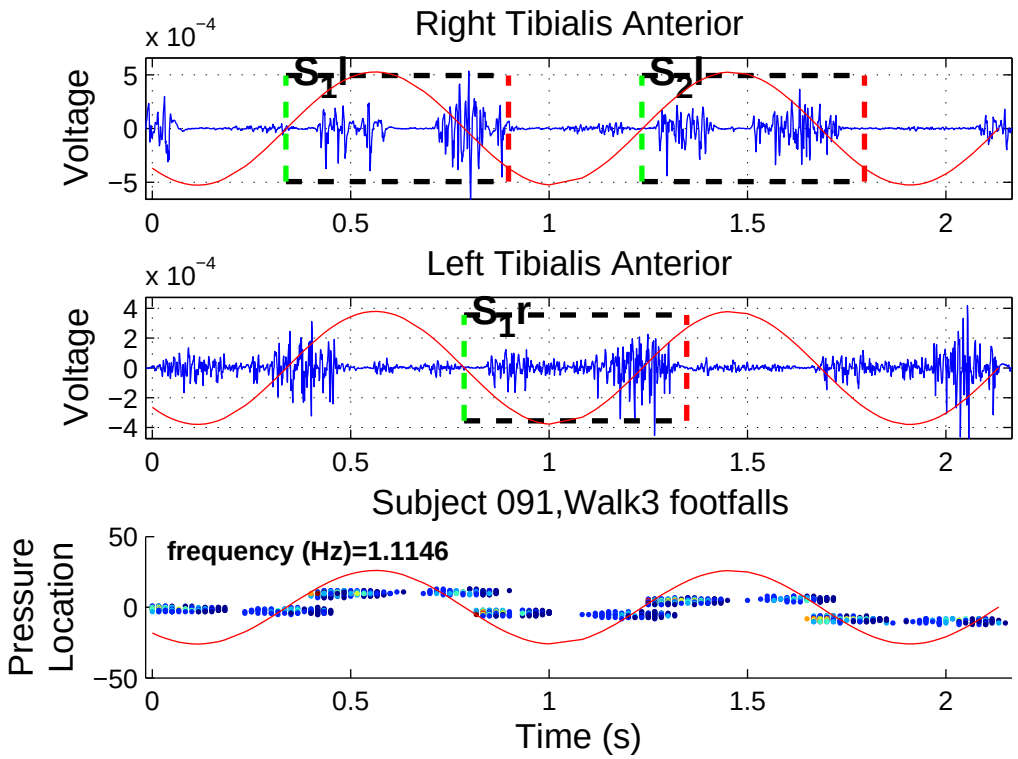

Figure 4.5: Subject 091, left and right tibialis anterior EMG with Gait-Sine estimate, muscle activation bounded by box

discussed in section 3.3. For this reason, a majority of metrics are designed based on changes in frequency, which should not change significantly with aging. Thus, it is reasonable to mix seniors and young in the control set.

Subjects under age 65 are subdivided into male ($N = 7, \overline{age} = 25.29, \sigma = \pm 3.82$) and female ($N = 13, \overline{age} = 26.77, \sigma = \pm 7.27$) sets, which represent the foundation of the control group. Additional control subjects are included by selecting those over age 65 with no reported history of hypertension, seizure, osteoporosis, diabetes, hypothyroidism, or neuropathy. Thus, the male ($N = 3, \overline{age} = 84.00, \sigma = \pm 6.24$) and female ($N = 7, \overline{age} = 89.71\sigma = \pm 10.45$) senior controls are established. Finally, the hypertensive set is subdivided by male ($N = 7, \overline{age} = 79.86, \sigma = \pm 8.05$) and female ($N = 17, \overline{age} = 82.24, \sigma = \pm 6.84$). Chapter 5 details the quantification of these groups, as well as the application of metrics and interpretation of the differences

between sets. To provide a visualization of these datasets, Figure 4.6 shows a Venn diagram for the male (left) and female (right) control (P_0, blue) and hypertensive (P_1, grey) sets.

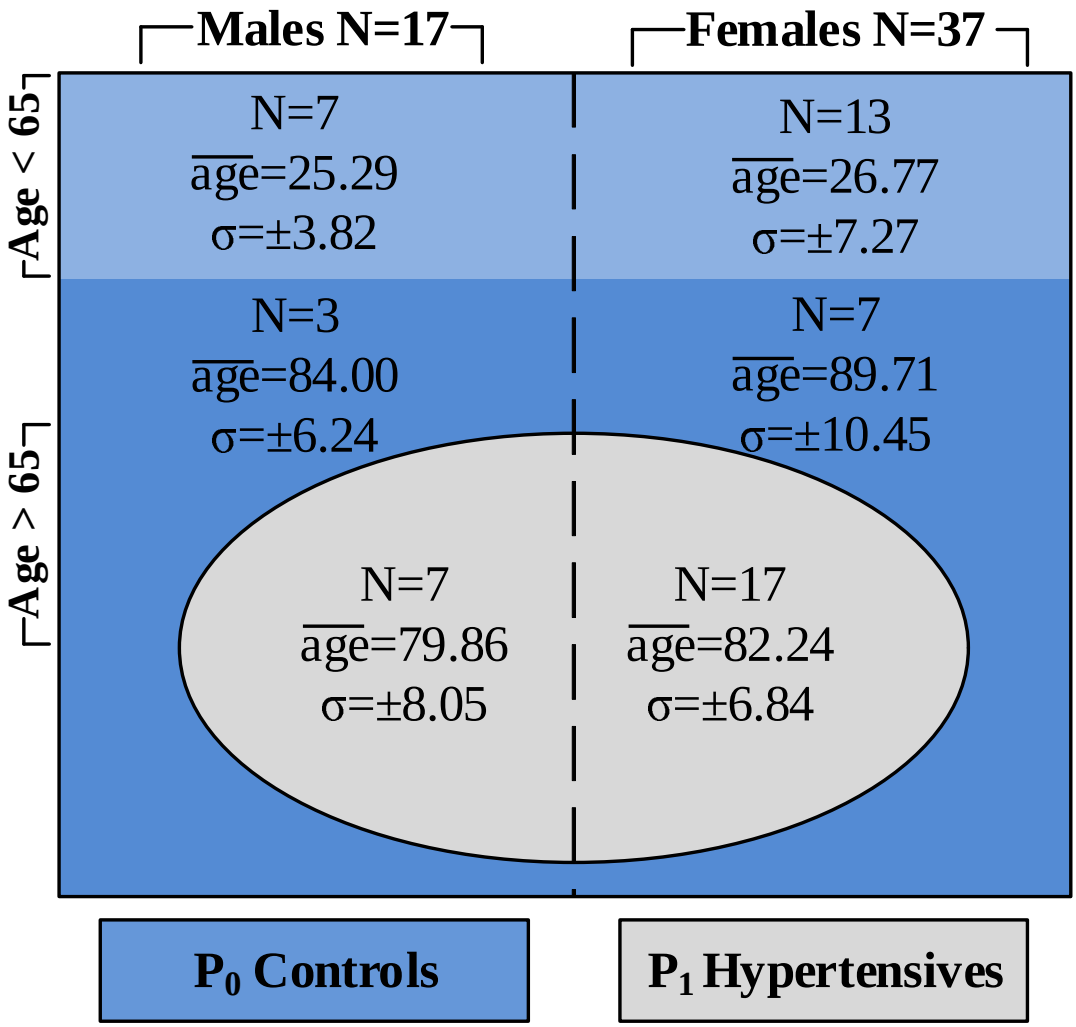

Figure 4.6: Diagram of population demographics for controls (P_0), shown as green, and hypertensives (P_1), shown as red, subdivided by age with number of subjects (N), mean age ($\overline{age}$) and variance (σ) shown

4.4 Data Pre-Treatment

Several steps are necessary before evaluating sEMG packets for comparison. First, distorted or poorly-recorded sEMG data must be rejected, which is done using sev-

eral standard criteria. Next, as discussed in section 4.2, sEMG signals are sorted and separated acording to the footfall pressure information and knowledge of muscular activation. These signal portions are then decomposed using time-frequency analysis, as described in section 4.5. After converting the sEMG signals to time-frequency distributions, key time-frequency characteristics are used to produce metrics, the mathematics and physiological foundation of which are described by section 3.3 Finally, these metrics are quantified using broad statistical interpretations. The procedure of statistical processing and the results are summarized in Chapter 5.

Data Rejection Procedure

As with any data acquisition undertaking, there are inevitably some errors in recording and equipment. Due to the arrangement of the experimental acquisition, recordings were not necessarily checked directly after recording. In light of this, software, hardware, and human error may contribute to unusable recordings; this is useful in that predictions can be made about how these data are corrupted. In order to rectify this problem, several steps are taken to reject data from final calculations before they are evaluated with time-frequency analysis.

Therefore, a procedure which rejects these data outright is desirable. The iterative Grubbs' test [60] follows a process to reject outlying data, and when coupled with relevant measures which are sensitive to badly recorded data, this test can quickly exclude bad data. The procedure is described by the inequality,

$$\frac{Y_{peak} - \overline{Y}}{s} > \frac{N-1}{N}\sqrt{\frac{t^2_{\alpha/2N,N-2}}{N-2+t^2_{\alpha/2N,N-2}}} \tag{4.1}$$

Where Y_{peak} represents an outlying data point, $\overline{Y}$ is the mean, s is the standard deviation, and $t^2_{\alpha/2N,N-2}$ is the critical value of the T-distribution at N-2 degrees of freedom. By use of this equation, values of Y_{peak} which exceed the critical value are

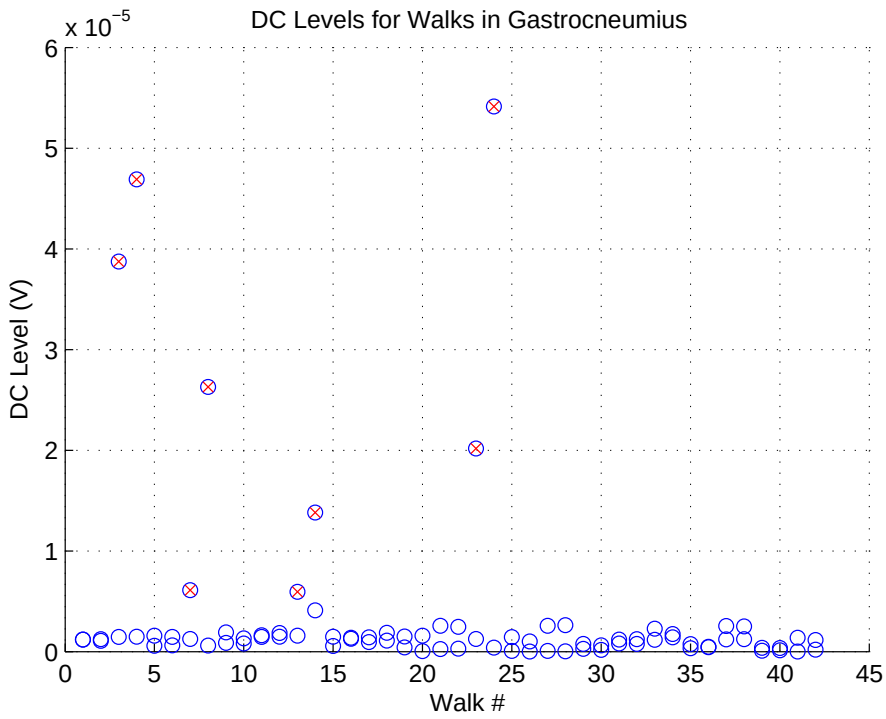

Figure 4.7: DC levels for male hypertensive-control subgroup walks with rejected sEMG data marked by x

rejected on their assumption as non-representative points. The process is iterative, so only those values selected by the critical value are included.

The criterion for rejection come from simple measures based the time-domain voltage recordings: signal energy, signal dc level, signal and peak-to-peak voltage. These measures are chosen with software, hardware, or user error in mind, as each of these represents commonly observed manifestations of these errors.

Additionally, the values for these measures should be consistent in typical sEMG signals within the population, assuming they are correctly recorded. As an example of this process, the male hypertensive-control subgroup walk DC levels are shown in Figure 4.7, along with several rejected points, which have extremely high dc levels compared to typical performance. These indicate bad connections to ground, and therefore unreliable recordings.

A low confidence interval of $\beta = 90\%$ is used, which takes a light-handed approach

to false negative rejection, yet excludes high outliers. After this rejection procedure, the remaining data is assumed to represent the populations in question, both control and hypertensive sets.

4.5 Application of Time-Frequency Analysis

As discussed in Chapter 2, time-frequency analysis represents a broad set of techniques, the results of which must be tailored and evaluated with the signals themselves in mind. Recall the sEMG signals represent the composite of independent muscle units producing impulse trains at varied frequencies and with varied wavelets due to tissue composition and distance. These impulse signal signatures differ due to the tissue channel between the muscle and the skin surface, which is akin to a type of filter. Thus, the signals recorded represent a heterogeneous composite of frequency, time, and amplitude components.

For this reason, time-frequency analysis provides a localization advantage that has not been present in the bulk of sEMG research. Key physiological information, such as muscle activation time, peak energy, peak frequency, or muscle firing density, can be quantitatively assessed directly from the time-frequency distributions. This allows for unique metric design that assess information pertaining to key physiological manifestations.

As with the musical example of Chapter 2, special consideration must be given to the selection of kernel, window size, and window type. As explained previously, the Hann-windowed reduced interference distribution ($\Phi_{RIDH}(t, \omega)$) performs extremely well with multicomponent signals at varying frequencies. As per the discussion in Chapter 3, sEMG signals are the definition of multicomponent, as the number of component signals is proportional to the number of recruited muscle fibers. However, window selections must still be made.

The RIDH uses a two-dimensional kernel, and therefore a two-dimensional window. As frequency localization is a slightly higher priority than time-localization (as this is done somewhat by the signal selection process), a Blackman time-domain window is used, while a Hamming window is used as the frequency-domain argument. This results in a slightly higher frequency resolution than time-resolution, but still eliminates a majority of cross-term artifacts.

Under normal gait times in both men and women see an upper maximal frequency of around 2.61 steps/s [61], it is reasonable to want several time sections of this. Using this figure results in an average step time for each foot of $t_{step} =^2 /_{2.61} = 761ms$. Using 10 time divisions in conjunction with (2.16)

$$N_t = \frac{761^{ms}/_{step}}{1ms}/(10 \times 1.44) \approx 53 \tag{4.2}$$

This result gives high resolution for each stride and simultaneously allows for a wide band of frequency calculation. For the frequency window, using the knowledge from section 3.3, each key area of the spectrum has a bandwidth of around $15Hz$. Recalling (2.16), a bandwidth of $1.44 * 15Hz$ should be sufficient to ascertain these key spectrum elements. Using these assumptions results in a frequency window size of

$$N_\omega = 1.44\frac{1000Hz}{15} \approx 96 \tag{4.3}$$

Thus, a high resolution is achieved with ample frequency width for analysis, which simultaneously isolates the key frequency areas of the expected sEMG spectrum. These parameters are used to create each time-frequency distribution of the relevant muscular activation windowed signals. After this process, there are several metrics which are used to distill the information of these distributions.

Table 4.2: Metrics summary

Metric Name (units)	Equation		Description
Instantaneous Time Duration (%)	$TD_{\%} = \frac{T}{t_g}$	(4.4)	Ratio of muscle activation time to localized gait window time
Local Frequency Bandwidth ($radians$)	$F_B = B = \sqrt{\frac{4\pi}{E}\int(\omega - \langle\omega\rangle)^2\lvert S(\omega)\rvert^2 d\omega}$	(4.5)	Frequency spreading across localized gait window
Local Frequency Maximum ($radians$)	$F_{max} = arg_\omega \max\{\lvert\Phi(t,\omega)\rvert\}$	(4.6)	Peak frequency within localized gait window
Energy Ratio Conditional (%)	$E_{\omega_b} = \frac{1}{E}\int_{-\infty}^{\infty}\int_{\omega_b}^{\infty}\Phi(t,\omega)d\omega dt$	(4.7)	Ratio of energy ratio above specific band to localized gait window energy
Conditional Energy from 40-100 Hz (%)	$E\%_{40-100Hz} = \frac{1}{E}\int_{-\infty}^{\infty}\int_{2\pi\times40}^{2\pi\times100}\Phi(t,\omega)d\omega$	(4.8)	Ratio of energy within contraction force [10] frequency bands to localized gait window energy
Energy Spectral Density (V^2)	$ESD_{40-100Hz} = \int\int_{2\pi\times40}^{2\pi\times100}\Phi(t,\omega)d\omega dt$	(4.9)	Energy spectra density within contraction force [10] frequency bands

4.6 Metric Design

The metrics by which to measure the possibility of relevant differens are based on the force-frequency relationships established previously. As per the discussion in section 3.3, one such area is the center sEMG muscular activation lobe between $40Hz$ and $100Hz$ [10]. The application of muscular force results in an increase in energy concentration within this band.

Time-frequency analysis of this changing frequency data has been applied to analyze lifting patterns [62] and gait [63] for analysis of changing muscle recruitment patterns. Thus, the metrics should reflect both this force-signal relationship, as well as information relevant to muscular activation during gait.

To help contextualize this section, four time-frequency plots footfalls from various subjects are shown in Figure 4.8 which represent the typical performance of the control and hypertensive subjects. Figures 4.8(a) and 4.8(b) show the vastus lateralis for control and hypertensive subjects, while Figures 4.8(c) and 4.8(d) show gastrocnemius footfalls. Finally, the mathematical representations and context of these metrics are summarized in Table 4.2 on page 56.

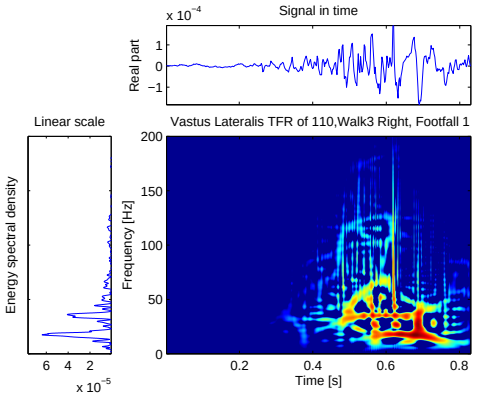

(a) Right vastus lateralis activation for (control case) subject number 110 waveforms

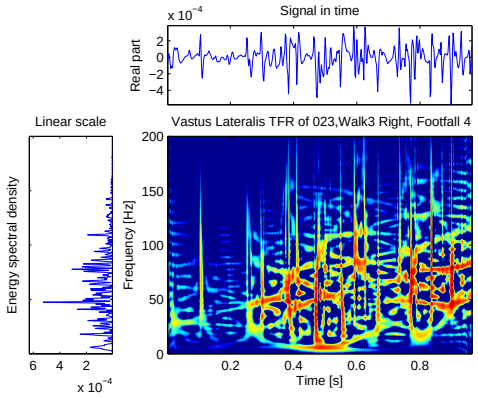

(b) Right vastus lateralus activation for (hypertensive case) subject number 023

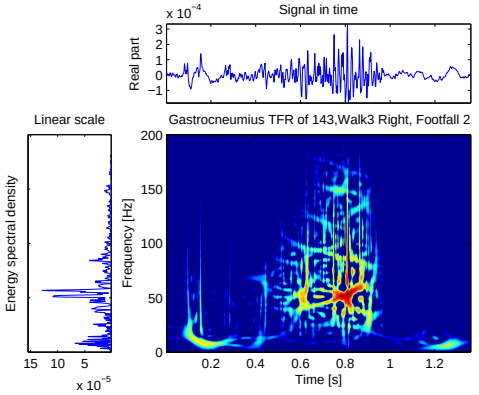

(c) Left gastrocnemius activation for (control case) subject number 143

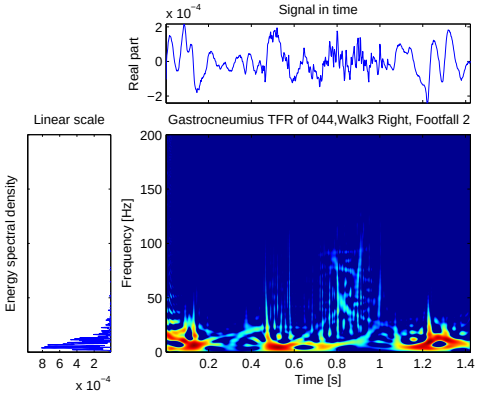

(d) Right gastrocnemius for (hypertensive case) subject number 044

Figure 4.8: Time-frequency distribution including energy spectral density and time-domain waveforms

- **Instantaneous Time Duration**

The instantaneous time duration metric corresponds to the time duration of muscular activation, based on the second moment of the time-domain signal, and evaluated in relation to the gait cycle portion. Recalling equation (2.7), for a signal $s(t)$, the metric is given by equation (4.4):

$$TD_{\%} = \frac{T}{t_g} = \frac{1}{t_g}\sqrt{\frac{4\pi}{E}\int t^2|s(t)|^2dt} \tag{4.4}$$

where t_g is the length of the windowed signal according to the gait cycle selection. Because the second time moment is divided by gait time, the metric represents a

percentage of gait cycle, rather than an exact time. This is done to correct for differing gait speeds, and thus represents the portion of the gait cycle over which the muscle operates.

In the context of the Figure 4.8, the control case of Figure 4.8(a) has a shorter signal time duration than the hypertensive case of Figure 4.8(b), corresponding to longer muscle activation and more energy use. In the gastrocnemius control and hypertensive cases shown in Figure 4.8(c) and Figure 4.8(d), the hypertensive case exhibits longer muscle contraction than the control case, as well as longer duration. Thus, time duration reflects extraneous muscle usage.

- **Local Frequency Bandwidth**

This metric uses the second frequency moment to determine the bandwidth of the signal, and is evaluated using the ratio to the Nyquist frequency. Thus, the metric reflects the frequency spreading caused by motor unit activation. Recalling (2.10) The metric is given by equation (4.5):

$$F_B = B = \sqrt{\frac{4\pi}{E}\int(\omega - \langle\omega\rangle)^2|S(\omega)|^2 d\omega} \tag{4.5}$$

where $S(f)$ is the Fourier transform of $s(t)$. Therefore, local frequency bandwidth is given in radians, and indicates the frequency spreading of muscular activation during walking.

Between Figure 4.8(a) and 4.8(b), the hypertensive case shows wider bandwidth in the vastus lateralis, while in the gastrocnemius muscle, there is wider spreading in the control case, Figure 4.8(c), than in the hypertensive case, Figure 4.8(d). Increased frequency spread reflects higher motor unit recruitment as explained in Chapter 3, and also corresponds to an increase in force [10]. This quantification serves as an indicator of leg muscle (and thereby gait) control, and serves as a highly sensitive metric for hypertension assessment.

• **Local Frequency Maximum**

Frequency maximum evaluates the frequency at which the peak energy occurs during activation. In comparison to the energy spectrum, this measures a signal's transient peak, rather than the marginal peak obtained through the summation of all frequency elements over the duration of the signal. This is given by equation (4.6):

$$F_{max} = \arg_{\omega} \max \{|\Phi(t, \omega)|\} \tag{4.6}$$

where $\Phi(t, \omega)$ is the instantaneous time-frequency distribution. As this is a frequency, its units are radians.

The hypertensive case for the vastus lateralis pictured in Figure 4.8(b) exhibits a higher frequency maximum than the control case of Figure 4.8(a), indicating an over-activation of motor units, rather than efficient use. For the gastrocnemius hypertensive case shown in Figure 4.8(d), the frequency maximum occurs lower, due to the extraneous muscle usage, while the control case, Figure 4.8(c) does not exhibit this characteristic. Thus, the metric is indicative of the sum effect of the muscle motor units' firing frequency, and where that energy is concentrated.

• **Energy Ratio Conditional**

This metric takes full advantage of time-frequency transformations of sEMG signals by comparing energy contained above a specific frequency and the total energy in each signal. This metric is similar to the frequency maximum metric; however, by comparing the total energy across the signal, it is less susceptible to anomalies in muscular activation. It is highly indicative of a statistically-relevant distinction between the control and experimental sets across several of the major muscle groups, and it is given by equation (4.7):

$$E_{\omega_b} = \frac{1}{E} \int_{-\infty}^{\infty} \int_{\omega_b}^{\infty} \Phi(t, \omega) d\omega dt \tag{4.7}$$

where

$$E = \int_{-\infty}^{\infty} |s(t)|^2 dt = \int_{-\infty}^{\infty} |S(f)|^2 df$$

is the total energy in the signal, and ω_b is the band of interest. For each set of data, frequency content is compared to the overall energy in the signal above the 20 Hz, 40 Hz, 60 Hz, 80 Hz, 100 Hz, and 120 Hz bands. By dividing the bounded energy by total energy, this metric represents a percentage.

When considering the two cases presented, it should be clear that the bands in which the energy is concentrated in shows a strong discrepancy between the control and hypertensive cases. In the hypertensive case, Figure 4.8(b), the vastus laturalis exhibits high energy concentration in higher frequency bands, whereas the control case, Figure 4.8(a) shows less energy at comparable frequencies. For the gastrocnemius pair, the unnecessary activations in the hypertensive case, Figure 4.8(d), mean a much lower frequency concentration of the energy as compared to the control case, 4.8(c).

- **Conditional Energy from 40-100 Hz**

Motor unit recruitment is concentrated within certain bands, from the 10-40 Hz range and around the 80 Hz range [10]. Thus, the energy contained in is energy band serves as another basis for comparison. To do this, energy across this bandwidth is normalized and compare to overall energy, as with the previous metric. The metric is given by equation (4.8) in terms of a ratio:

$$E\%_{40-100Hz} = \frac{1}{E} \int_{-\infty}^{\infty} \int_{2\pi\times 40}^{2\pi\times 100} \Phi(t,\omega) d\omega dt \tag{4.8}$$

Much like the instantaneous frequency bandwidth metric, for the vastus lateralis control case in Figure 4.8(a), there is little spreading, but for the hypertensive case shown in 4.8(b), there is more energy spread across this band in relation to the overall energy. Likewise, for the gastrocnemius control case in Figure 4.8(c), energy is highly

concentrated from 40-100 Hz, but is concentrated at much lower frequencies in the hypertensive case, shown in Figure 4.8(d).

- **Energy Spectral Density**

The final metric uses the energy spectral density of the 40-100 Hz band to assess signal energy. Thus, it is unique, as it is not a ratio to overall energy in the windowed signal. Therefore, this metric is thus susceptible to subject physiology, which may reduce the energy present in the sEMG signal, but is useful as a measure between subjects with similar physiology. The metric is given by equation (4.9) in terms of energy (V^2):

$$ESD_{40-100Hz} = \int_{2\pi\times 40}^{2\pi\times 100} \Phi(\omega) d\omega \tag{4.9}$$

where $\Phi(\omega)$ is the ESD of the windowed signal:

$$\Phi(\omega) = \left| \frac{1}{\sqrt{2\pi}} \int_{-\infty}^{\infty} s(t) e^{-i\omega t} dt \right|^2 = \frac{S(\omega) S^*(\omega)}{2\pi}$$

For the cases pictured above, in both control cases of Figs. 4.8(a) and 4.8(c), the energy spectral density, shown on the left, is on a smaller order of magnitude than that of the hypertensive cases in Figs. 4.8(b) and 4.8(d). As energy in this band roughly corresponds to force, a larger amount of energy in this band corresponds to increased force of muscular activation.

4.7 Summary

In this chapter, the key aspects of the experimental setup and procedure were discussed. The fundamental concept is the use of the sEMG sensors in conjunction with the pressure sensitive mat, and the extension of the gait-sine algorithm for footfall separation. This process allows for the use of metrics which operate on the gait-aligned signals for various groups. Thus, a direct comparison of metric

information can be compared across populations and groups. In the next chapter, the results of these metrics will be discussed from the perspective of two key sub-populations: hypertensive and non-hypertensive subjects.

Chapter 5

Results

This chapter lays out the results of comparison between two focus populations in the experiment: hypertensive and non-hypertensive. In order to make this comparison, a small background in the statistical methods used is necessary. These methods will be discussed in section 5.1.

5.1 Statisitcal Evaluation

In order to properly differentiate between hypertensive and nonhypertensive groups, a binary hypothesis test is used for differentiation. There are four distinct subsets; two for male and female, as well as non-hypertensive (P_0) subjects and hypertensive (P_1) subjects. Each subject in these subsets are used to create values representative of the subject using the aforementioned metrics, for each of the four muscle groups. Each metric's value is notated as $x_{\langle m \rangle}$, and belongs to either P_0 or P_1. Then, for the set of metric values $x_{\langle m \rangle}$, a normal distribution may be calculated:

$$f(x_{\langle m \rangle}, \mu_{\langle m \rangle}, \sigma^2_{\langle m \rangle}) = \frac{1}{\sqrt{2\pi\sigma^2_{\langle m \rangle}}} e^{\frac{-\left(x_{\langle m \rangle} - \mu_{\langle m \rangle}\right)^2}{\sigma^2_{\langle m \rangle}}} \tag{5.1}$$

where $\mu_{\langle m \rangle}$ is the mean of $x_{\langle m \rangle}$ and $\sigma^2_{\langle m \rangle}$ is the variance.

These normal distributions are treated as having varying average values, and thus a threshold α may be used as a binary test value. Choosing a threshold α that exists at the weighted mean of the two values is analogous to the minimal probability of

error, which minimizes false positives and false negatives. The value of α is thus

$$\alpha = \frac{\mu_{\langle m \rangle, C} \times \sigma^{-2}_{\langle m \rangle, C} + \mu_{\langle m \rangle, E} \times \sigma^{-2}_{\langle m \rangle, E}}{\sigma^{-2}_{\langle m \rangle, C} + \sigma^{-2}_{\langle m \rangle, E}} \tag{5.2}$$

where C and E refer to the control and experimental means (μ) and standard deviations σ^2 for each metric $\langle m \rangle$. Meanwhile, the probability of error, P_e in the general case is given by:

$$P_e = P(H_1|H_0)P(H_0) + P(H_0|H_1)P(H_1) \tag{5.3}$$

Thus, using the weighted means from $p(H_0)$ and $p(H_1)$ to determine (α) results in the minimum number of false calls. The detector decides a positive case for a random variable x using

$$p(x|H_1) > p(x|H_0) \tag{5.4}$$

Therefore, the detector employed is a maximum likelihood detector, which maximizes $p(x|H_n)$ and minimizes P_e. Thus, this threshold also the point at which the probability of type I and type II errors are both minimized. Once these threshold values are calculated for each metric, they may be used to assess per-subject metric values. Next, for each subject sn, metric scores $\mathbf{x}_{sn,\langle m \rangle}[n]$ are calculated for each footfall $[n]$.

In order to make meaningful sense of the relationships between these populations, the per-footfall probabilities are aggregated, representing in a per-subject total metric score, $T_{sn,\langle m \rangle}$, given by equation (5.5):

$$T_{sn,\langle m \rangle} = \frac{\sum_{N=1}^{N_{footfall}} \mathbf{x}_{sn,\langle m \rangle}[n]}{N_{footfall}} \tag{5.5}$$

where $N_{footfall}$ is the number of footfalls for the subject, $\mathbf{x}_{sn,\langle m \rangle}[n]$ is the metric value for each footfall $[n]$.

For a subject sn in P_0, a false positive (FP) or type I error occurs when $T_{sn,\langle m \rangle} > \alpha_{\langle m \rangle}$, or a true negative (TN) when $T_{sn,\langle m \rangle} < \alpha_{\langle m \rangle}$, . These values are based on a

higher experimental group mean, $H_1 : \mu_{\langle m \rangle} > H_0 : \mu\langle m \rangle$, where $\mu\langle m \rangle$ is the mean of the normal distributions for P_0 and P_1 , for the specific metric $\langle m \rangle$. Likewise, for a subject sn in P_1, a true positive (TP) occurs when $T_{sn,\langle m \rangle} > \alpha_{\langle m \rangle}$, and a false negative (FN), or type II error, assuming a higher experimental mean $T_{sn,\langle m \rangle} < \alpha_{\langle m \rangle}$. Thus, probability of each footfall is assessed in the context of a subject.

The relationship between the mean values comes into play in sections 5.2 and 5.3, as some metric/muscle groups may have higher or lower means between subsets. These are indicated either by + or − in Tables 5.1(b) and 5.2(b).

The efficacy of each metric at distinguishing between populations follows a straightforward method of calculation. At each metric threshold $\alpha_{\langle m \rangle}$, FP, FN, TP, and TN are calculated. From here, the accuracy (ACC), true positive rate (TPR) and true negative rate (TNR) may be calculated by their definitions.

$$ACC(\alpha_{\langle m \rangle}) = \frac{TP(\alpha_{\langle m \rangle}) + TN(\alpha_{\langle m \rangle})}{P + N} \tag{5.6}$$

$$TPR(\alpha_{\langle m \rangle}) = \frac{TP(\alpha_{\langle m \rangle})}{TP(\alpha_{\langle m \rangle}) + FN(\alpha_{\langle m \rangle})} \tag{5.7}$$

$$TNR(\alpha_{\langle m \rangle}) = \frac{TN(\alpha_{\langle m \rangle})}{TN(\alpha_{\langle m \rangle}) + FP(\alpha_{\langle m \rangle})} \tag{5.8}$$

As an example for one metric, A visualization of the procedure is shown by Figure 5.1, beginning with obtaining the optimal threshold α, assessment of population footfalls, and the aggregation of the results across metrics and muscle groups. This process therefore involves several parallel steps which result in a final measure of sensitivity and specificity for a population.

Finally, Bayesian risk is used to assess overall subject score. This is achieved by extending (5.5) to all metrics which have an accuracy of 60% or higher. Thus, metrics which show reduced ability to differentiate between populations are discarded. Using equation 5.9, a cost risk of 1 is assigned in the case of accuracy above 60% and 0 when accuracy is below 60%:

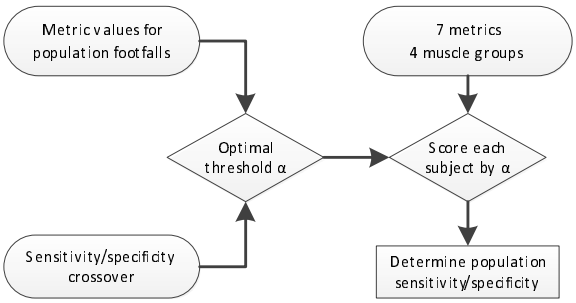

Figure 5.1: Flowchart for assessment of metric sensitivity between populations

$$Score = \mathcal{R} = \sum_{i=0}^{M-1} \sum_{j=0}^{M-1} C_{ij} P(H_i|H_j) P(H_j) \tag{5.9}$$

Where C_{ij} is the cost matrix. Thus, based on the metric distributions of each population, subjects are evaluated by the relationship to these probabilities.

5.2 Male Control vs Male Hypertensive

The first subset to examine is that of the males, who have a smaller and more straightforward evaluation than the females. The male control set consists of young males and control senior subjects ($N = 10, \overline{age} = 42.9, \sigma = \pm 28.68$). The experimental set consists of the hypertensive subjects described in section 4.3 ($N = 7, \overline{age} = 79.86, \sigma = \pm 8.05$). Table 5.1(a) gives the metric accuracy scores for muscle group, though including only $E_{\omega_b=40}$ and $E_{\omega_b=120}$, while Table 5.1(b) shows the respective values for interpretation. In the case of Table 5.1(b), the + and - refer to the comparison of metric values in the control group to those of the experimental group. For example, the male tibialis anterior $TD_{\%}$ metric has a value of 7.078%. The + indicates that the control group's metric scores are lower than this value, while the experimental group are above.

By the use of equation (5.5), the metrics with optimal accuracy are $TD_{\%}$, F_B, F_{max}, $E_{\omega_b=120Hz}$, and $ESD_{40-100Hz}$, for gastrocnemius, vastus lateralis, and tibialis anterior,

Table 5.1: Metric and muscle values for male subsets

(a) Accuracy levels

Muscle	$TD_{\%}$	F_B	F_{max}	$E_{\omega_b=40Hz}$	$E_{\omega_b=120Hz}$	$E\%_{40-100Hz}$	$ESD_{40-100Hz}$
Tibialis Anterior	**75.00**	**76.92**	**62.50**	**62.50**	**76.92**	**62.50**	53.85
Gastrocneumius	**62.50**	**76.92**	**62.50**	**62.50**	**76.92**	**62.50**	**75.00**
Vastus Lateralis	**69.23**	**69.23**	**76.92**	**75.00**	**76.92**	53.85	**69.23**
Biceps Femoris	**62.50**	**62.50**	53.85	**62.50**	**62.50**	53.85	53.85
Aggregates	Acc: 94.12%, TPR: 100.00%, TNR: 85.71%						

***Measures with accuracy above 60% highlighted**

(b) Metric crossover values

Muscle	$TD_{\%}$ (%)	F_B (Hz)	F_{max} (Hz)	$E_{\omega_b=40Hz}$ (%)	$E_{\omega_b=120Hz}$ (%)	$E\%_{40-100Hz}$ (%)	$ESD_{40-100Hz}$ (mV^2)
Tibialis Anterior	7.078+	31.93-	74.45-	88.15+	39.62-	41.11+	329.04-
Gastrocneumius	13.13+	17.56-	57.97-	75.78-	20.26-	40.42-	317.00-
Vastus Lateralis	10.19+	23.20-	47.02-	67.95-	18.52-	49.67-	358.37-
Biceps Femoris	19.58+	13.33+	23.12-	52.31-	16.35-	37.70-	307.56-

***+/- indicates experimental group metric values lie above or below control group**

all of which show high ($> 75\%$) levels of accuracy. From inspection of Table 5.1(a), one key point is that the tibialis anterior exhibits several measures which are sensitive to hypertension, with a majority of metrics showing high accuracy, except in the case of $ESD_{40-100Hz}$. It should also be noted that the energy ratio conditional ($E_{\omega_b=120}$) shows high accuracy levels. Finally, the biceps femoris exhibit much lower levels of accuracy to the presence of hypertension ($< 63\%$), to the point that it barely rejects the null hypothesis in some cases.

In the case of the $TD_{\%}$ and F_B metrics, it is clear from Table 5.1(b) that the control group exhibits a longer time duration and a lower frequency bandwidth. Considering the discussions of sections 3.3 and 3.5, these characteristics can be explained in terms of a shorter but more rapid firing, with energy becoming concentrated in a narrower bandwidth. Thus, these metric values are indicative of muscular recruitment.

Additionally, the $E_{\omega_b=120Hz}$ metric values, and the $ESD_{40-100Hz}$ metric values all show higher valuation in the control groups when compared to the experimental groups. This can be interpreted as a higher frequency center, such that energy in the main band is slightly higher in frequency. This notion is backed up when examining the values for maximum frequency (F_{max}), which all show higher values in the control group compared to the experimental. Especially in the tibialis, where the crossover

point is at 74.45 Hz, these high frequency maximums represent large numbers of motor unit recruitment.

After evaluating the aggregate score by the Bayes risk, it is straightforward to determine the confusion matrix based on the relationship between scores. These values are used to create Figure 5.2(a), which displays a histogram of the scores. True and false negatives lie to the left of .5, while true and false positives are to the right. By evaluating these values, giving accuracy as 94.12% , true positive rate as 100%, and true negative rate as 85.71%. Additionally, Figure 5.3(a) shows these valuations, which expands the results across the subjects themselves. The x-axis of these figures reference young controls 'y', senior controls 's', and experimental subjects 'e'.

In Figure 5.2(a), there is one false negative, subject 51. However, this subject's aggregate metric score is extremely close to the midpoint threshold for declaring positive or negative, as is clear in Figure 5.3(a). Additionally, there is no indication from his medical history that should explain this issue. It is, however, an outlier from the main group of hypertensive subjects, whose score is generally much higher. Additionally, using the standard deviation as a reference, the score for this subject shows a wide spread across the metrics used to analyze. Thus, it is fair to assume that this case would merit further investigation in a clinical setting.

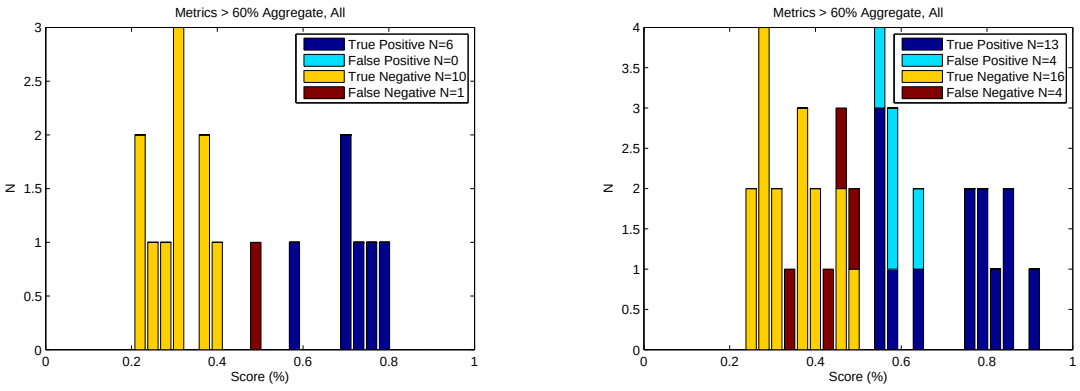

(a) Male subset (b) Female subset

Figure 5.2: Histogram of aggregated metric scores for female control vs hypertensive, by confusion matrix score

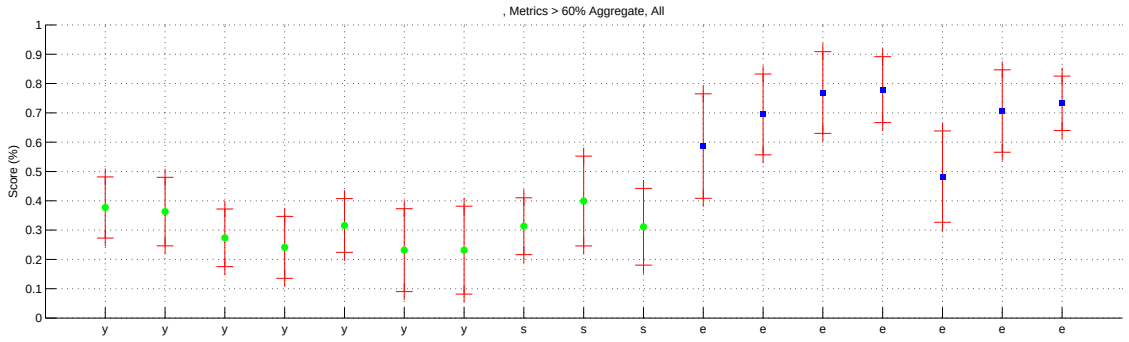

(a) Male subset

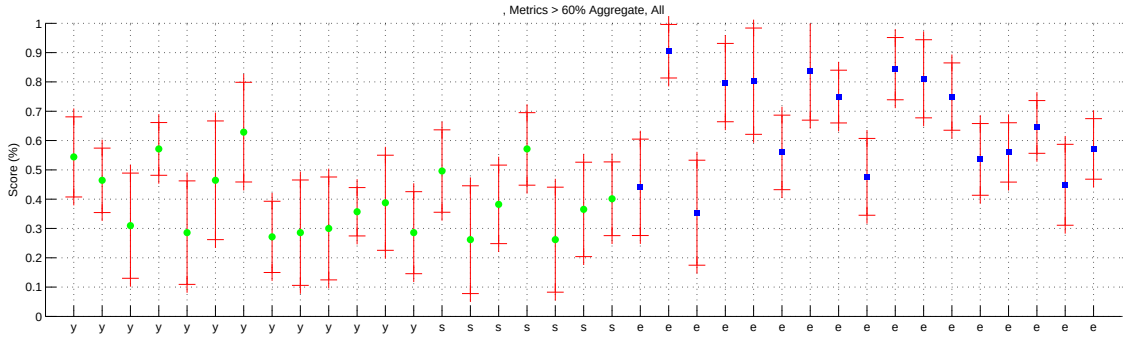

(b) Female subset

Figure 5.3: Aggregated metric scores by subject number, controls represented by green, hypertensives represented by blue, with error bars corresponding to $\pm\frac{\sigma}{2}$ for aggregate score, x axis 'y' refers to young control, 's' refers to senior control, 'e' refers to experimental

5.3 Female Control vs Female Hypertensive

Next, the female set is examined. The control group P_0 consists of the young and old females ($N = 20, \overline{age} = 48.80, \sigma = \pm 31.89$), which contain several senior controls as described by section 4.3. Meanwhile the hypertensive group P_1 has a slightly higher average age when compared to the males ($N = 17, \overline{age} = 82.24, \sigma = \pm 6.84$).

Table 5.2(a) shows the accuracy levels for the different metric/muscle groups, again including only $E_{\omega_b=40}$ and $E_{\omega_b=120}$ from the energy bandwidth conditional metric. It is immediately apparent that the overall level of accuracy between females is lower compared to the male subgroup accuracy levels of Table 5.1(a). However, some

Table 5.2: Metric and muscle values for female subsets

(a) Accuracy levels for metric and muscle female subsets

Muscle	$TD_{\%}$	F_B	F_{max}	$E_{\omega_b=40Hz}$	$E_{\omega_b=120Hz}$	$E\%_{40-100Hz}$	$ESD_{40-100Hz}$
Tibialis Anterior	**66.67**	58.33	**63.16**	**68.42**	**63.16**	54.17	**63.16**
Gastrocneumius	**63.16**	54.17	58.33	54.17	54.17	58.33	58.33
Vastus Lateralis	54.17	52.63	54.17	54.17	**63.16**	58.33	47.37
Biceps Femoris	58.33	58.33	52.63	**63.16**	54.17	54.17	54.17
Aggregates	Acc: 78.38%, TPR: 80.00%, TNR: 76.47%						

***Measures with accuracy above 60% highlighted**

(b) Metric crossover values

Muscle	$TD_{\%}$ (%)	F_B (Hz)	F_{max} (Hz)	$E_{\omega_b=40Hz}$ (%)	$E_{\omega_b=120Hz}$ (%)	$E\%_{40-100Hz}$ (%)	$ESD_{40-100Hz}$ (mV^2)
Tibialis Anterior	14.14+	20.11-	42.83-	72.79-	26.90-	53.12-	367.90-
Gastrocneumius	21.41+	12.75-	21.24-	49.91-	18.28-	41.71-	253.74-
Vastus Lateralis	23.09-	12.75-	20.75-	38.40+	12.73-	29.21+	235.66-
Biceps Femoris	22.96-	13.73+	21.70+	42.00+	14.14+	34.25+	251.33+

***+/- indicates experimental group metric values lie above or below control group**

measures still show high levels of distinction between control and experimental sets.

For the females, the tibialis anterior muscle shows consistently high accuracy when distinguishing the presence of hypertension, especially in the $TD_{\%}$, F_{max}, $E_{\omega_b=40Hz}$, $ESD_{40-100Hz}$ metrics. The $E_{\omega_b=40Hz}$ metric also shows relatively high accuracy in the biceps femoris, while $E_{\omega_b=120Hz}$ shows similar accuracy in the vastus lateralis. It should also be noted that the energy ratio conditional shows the highest discrepancy at 40 Hz in the tibialis anterior and biceps femoris muscle, compared to the males which show higher discrepancies at 120 Hz. Explanation of these male-female discrepancies are discussed in section 5.4.

When comparing the values of Table 5.2(b) to those of the male values of Table 5.1(b), the reason for the distinction should be clear. In the tibialis anterior and gastrocnemius, the $TD_{\%}$ metric, while having the same relationship between experimental and controls, is much higher (14.14% for females vs. 7.08% for the males in the case of the tibialis). Likewise, the bandwidth is smaller for the females than in the males. This results in similar metrics performing well, but an overall loss in fidelity, due to a smaller margin of discrepancy between control and experimental metric group values.

Additionally, it is interesting that $E_{\omega_b=40Hz}$ in the tibialis gives superior perfor-

mance. This suggests a lower overall frequency, making a comparison at the low-energy levels more useful in determining differences than a higher frequency. This notion is borne out when comparing the levels of F_{max}, in which the frequencies in the females are lower on the whole. Finally, in the $ESD_{40-100Hz}$ metric, the overall energy levels are lower in females. The reasons for these difference lie in key physiological discrepancies between males and females, discussed in section 3.3, and will be explored in the context of the research in section 5.4.

Figure 5.2(b) shows a histogram arrangement of the confusion matrix, which corresponds to an accuracy of 78.38%, a true positive rate of 80.00%, and a true negative rate of 76.47%. When comparing these to Figure 5.3(b), these values make sense. On close inspection of those false positives and negatives, they are similar to the false negative of the male case. A majority of these cases lie near the center point of the crossover, and the standard deviation of the metric spreading implies that these subjects may not be reliably placed in either category. Thus, further investigation is necessary to determine confounding factors which may affect the accuracy of the test. Also similar to the male subgroup, several hypertensive cases ($N = 9$) lie above .7, and likewise several true negatives ($N = 13$) lie below .4. Thus, it may be inferred that the test is highly accurate in a majority of the hypertensive cases.

5.4 Discussion

From the evaluation of the male and female subsets, several clear trends exist, which are made apparent by close investigation of Tables 5.1(a) and5.2(a). As stated previously, in the male subset, while gastrocnemius and vastus lateralis muscles show high accuracy levels across several metrics, the female gastrocnemius and vastus lateralis show much lower ($< 60\%$) sensitivity to the presence of hypertension when compared to male subjects. Conversely, the tibialis anterior muscles shows much

higher relative accuracy levels in the female subset than in the male subset.

Another key difference is clear in the energy ratio metric (E_{ω_b}), discussed in section 4.6. This metric evaluates the ratio of energy contained above a specific band (high frequency) compared to overall energy, and is shown in the tables at $E_{\omega_b=40}$ and $E_{\omega_b=120}$. In the male subset, the use of 120 Hz for the low-band cutoff resulted in the highest accuracy for detection of hypertension in the tibialis anterior, gastrocnemius, and vastus lateralis. Conversely for the females, in the tibialis anterior, biceps femoris, the 40 Hz cutoff showed the highest levels of accuracy. These differences are attributed to fundamental physiological differences between male and female groups: subcutaneous tissue distribution and musculature differences.

The underpinnings of these male and female physiological differences were discussed in section 3.3. As discussed there, males tend to have a wider sEMG bandwidth due to lower subcutaneous tissue levels and higher muscle mass. This results in a greater clarity and lower mean frequency of activation, in comparison to females. Additionally, as discussed, key differences in walking patterns in females cause the use of certain muscles to differ. This may serve to explain the discrepancies between measurement abilities between the male and female muscle groups, and especially in the tibialis anterior muscle [45]. Thus, it stands to reason that the tibialis anterior would give more precise results in the female sets, as is the case.

As noted previously, those metrics which show high accuracy in distinguishing between male and female subgroups are highly correlated to the frequency content of the signal, especially bandwidth (F_B) or energy ratio conditional (E_{ω_b}). This is especially telling when noting that in the female subset, the band comparison at $\omega_b = 40Hz$ is more indicative, while in males $\omega_b = 120Hz$ shows more discrepancy, save for the vastus lateralis muscle. In conclusion, although there are differences in accuracy levels between male and female groups due to a variety of factors, from physiological gender differences to muscle usage, there are still clear distinctions between

the hypertensive and non-hypertensive groups which are measurable and quantifiable directly from the gait sEMG signals.

Chapter 6

Conclusion

In this work, I have endeavored to give an account of the background, as well as the application, of several major topics, for the purpose of a noninvasive evaluation of gait. This work is made necessary by the risk of our senior population to falling, and seeks to provide one more tool in a growing array of diagnostic tools which can alter the course of seniors' lives for the better. Additionally, it serves as an area for intersection of the fields of biomedicine with electrical engineering, using old tools to solve new tasks, each of which have a rich history.

Chapter 2 took an in-depth look into the concepts of signal analysis in the frequency domain revealed key shortcomings in old methods. The Fourier transform, while useful when evaluation stationary signals, is not extremely useful for transient signals, such as sEMG signals during gait. And while there is extensive work on sEMG spectrum analysis, there is comparatively less work when evaluating these transient signals.

The investigation into sEMG signals necessitated a wider background on human physiology. In Chapter 3, the background for the sEMG signal was established, which took a deep look into the effects that physiology, age, and gender might have on the signals themselves. These were interpreted in the context of their frequency spectrum, which included the state of the art of sEMG analysis. Finally, these signals were discussed in the context of typical human gait.

The concepts of chapters 2 and 3 were extended to the experimental setup in Chapter 4. This chapter developed a wide array of concepts, applying spectral anal-

ysis to the time-varying gait signals. Of primary importance here was the use of the gait-sine algorithm, which exploits the natural sinusoidal sway of the center of mass to extrapolate the gait cycle from footfall pressure data. These gait points were used to slice sEMG signals for analysis via metrics based on the classical spectral measurement techniques.

Finally, these metrics were applied to identify discrepancies between hypertensive and control sets. These results were based on a large database which recruits from a variety of subjects. Many investigations of sEMG signals rely a small number of candidates, but by use of the gait-sine algorithm, muscle activation can be compared directly, contextualized by gait cycle. Thus, statistical analysis was straightforward, and does not rely on a small sample set for control and test case comparison.

The overall goal of this research was to provide a quantitative tool for medical practitioners, including doctors, therapists, and clinicians, to evaluate comorbidities with additional quantitative insight. This work is part of the continuing effort to provide an additional tool to assess geriatric patients, their health levels, and thus, their risk for falling. By taking these findings as a basis for future work, this clinical assessment of hypertension can be made by comparing the aggregated database results to a clinical patient to screen for hypertension. With extremely high accuracy, and high true positive rates, the use of this method to corroborate clinician findings should be readily apparent.

The future of this research will focus on additional methods to aggregate data in a meaningful way, both by examining outliers and using comparisons of a subjects' footfalls to one another to create a more accurate snapshot for overall comparison. Additionally, other conditions which predict fall risk will be examined in the future, but as hypertension is common among US seniors, it serves well as an initial point of investigation. Finally, while gait has been researched for many years, there have been very few studies with an experimental setup that effectively corroborates gait

and EMG signals for analysis. While this apparatus has been focused as a diagnostic tool for seniors, it has potential in the fields of sports medicine and physical therapy as a diagnostic tool for gait activation points, muscle distributions, and identification of other neuropathies. Thus, this research holds promise, both for the state of clinical medicine as well as for furthering knowledge of non-stationary signals during gait.

Thank you.

Bibliography

[1] J. B. J. b. Fourier, *Théorie analytique de la chaleur*, fr. Chez Firmin Didot, père et fils, 1822.

[2] J. Ville, "Théorie et applications de la notion de signal analytique", French, *Cables et Transmissions*, vol. 2A, no. 1, pp. 61–74, 1948.

[3] J. Jeong and W. Williams, "Kernel design for reduced interference distributions", *IEEE Transactions on Signal Processing*, vol. 40, no. 2, pp. 402–412, 1992, ISSN: 1053-587X. DOI: 10.1109/78.124950.

[4] L. Cohen, "Time-frequency distributions-a review", *Proceedings of the IEEE*, vol. 77, no. 7, pp. 941–981, Jul. 1989, ISSN: 0018-9219. DOI: 10.1109/5.30749.

[5] M. Piccolino and M. Bresadola, "Drawing a spark from darkness: john walsh and electric fish", *Trends in Neurosciences*, vol. 25, no. 1, pp. 51–57, Jan. 2002, ISSN: 0166-2236. DOI: 10.1016/S0166-2236(00)02003-8. [Online]. Available: http://www.sciencedirect.com/science/article/pii/S0166223600020038 (visited on 02/10/2014).

[6] L. Galvani, *De viribus electricitatis in motu musculari commentarius*, en. Elizabeth Licht, Publisher, 1953.

[7] "A translation of luigi galvani's de viribus electricitatis in motu musculari commentarius. commentary on the effect of electricity on muscular motion", *Journal of the American Medical Association*, vol. 153, no. 10, pp. 989–989, Nov. 1953, ISSN: 0002-9955. DOI: 10.1001/jama.1953.02940270095033. [Online]. Avail-

able: http://dx.doi.org/10.1001/jama.1953.02940270095033 (visited on 02/10/2014).

[8] A. Volta, B. Dibner, and V. Antinori, *Collezione dell' opere del cavaliere Conte Alessandro Volta ..* ita. Firenze : Nella stamperia di G. Piatti, 1816. [Online]. Available: http://archive.org/details/collezionedellop21volt (visited on 02/10/2014).

[9] E. H. Du Bois-Reymond, B. Jones, and J. H. J. Müller, *On animal electricity: being an abstract of the discoveries of Emil Du Bois-Reymond ..* eng. London, J. Churchill, 1852. [Online]. Available: http://archive.org/details/onanimalelectri00boisgoog (visited on 02/10/2014).

[10] J. Basmajian and C. De Luca, *Muscles Alive: Their Functions Revealed by Electromyography*, 5th. Baltimore, United States: Williams and Wilkins, 1985.

[11] H. S. Gasser and J. Erlanger, "A study of the action currents of nerve with the cathode ray oscillograph", en, *American Journal of Physiology – Legacy Content*, vol. 62, no. 3, pp. 496–524, Nov. 1922, ISSN: 0002-9513, [Online]. Available: http://ajplegacy.physiology.org/content/62/3/496 (visited on 02/17/2014).

[12] D. S. McKenzie, "The russian myo-electric arm", en, *Journal of Bone & Joint Surgery, British Volume*, vol. 47-B, no. 3, pp. 418–420, Aug. 1965, ISSN: 2049-4394, 2049-4408. [Online]. Available: http://www.bjj.boneandjoint.org.uk/content/47-B/3/418 (visited on 02/18/2014).

[13] G. Wei, Q. Sun, G. Tang, X. Xie, A. Ni, and F. Tian, "A novel muscle force model based on the fuzzy theory", in *2010 Seventh International Conference on Fuzzy Systems and Knowledge Discovery (FSKD)*, vol. 3, 2010, pp. 1163–1166. DOI: 10.1109/FSKD.2010.5569155.

[14] D. Staudenmann, I. Kingma, A. Daffertshofer, D. F. Stegeman, and J. H. V. Dieën, "Improving EMG-Based muscle force estimation by using a high-density EMG grid and principal component analysis", *IEEE Transactions on Biomedical Engineering*, vol. 53, pp. 712–719, 2006.

[15] D. Staudenmann, A. Daffertshofer, I. Kingma, D. F. Stegeman, and J. H. v. Dieën, "Independent component analysis of high-density electromyography in muscle force estimation", *IEEE Transactions on Biomedical Engineering*, vol. 54, pp. 751–754, 2007.

[16] C. K. Jablecki, M. T. Andary, Y. T. So, D. E. Wilkins, and F. H. Williams, "Literature review of the usefulness of nerve conduction studies and electromyography for the evaluation of patients with carpal tunnel syndrome", *Muscle & Nerve*, vol. 16, pp. 1392–1414, 1993.

[17] R. F. Duyffa, J. V. d. Boschc, D. M. Lamanb, B.-J. P. v. Loonc, and W. H. J. P. Linssena, "Neuromuscular findings in thyroid dysfunction: a prospective clinical and electrodiagnostic study", *J Neurol Neurosurg Psychiatry*, vol. 68, pp. 750–755, 2000.

[18] B. H. Jansen, V. H. Miller, D. C. Mavrofrides, and C. W. S. Jansen, "Multidimensional EMG-Based assessment of walking dynamics", *IEEE Transactions on Neural Systems and Rehabilitation Engineering*, vol. 11, pp. 294–300, 2003.

[19] P. Bonato, S. H. Roy, M. Knaflitz, and C. J. De Luca, "Time-frequency parameters of the surface myoelectric signal for assessing muscle fatigue during cyclic dynamic contractions", *IEEE Transactions on Biomedical Engineering*, vol. 48, pp. 745–755, 2001.

[20] G. De Michele, S. Sello, M. C. Carboncini, B. Rossi, and S.-K. Strambi, "Cross-correlation time-frequency analyisis for multiple EMG signals in parkinson's

disease: a wavelet approach", *Medical Engineering & Physics*, vol. 25, pp. 361–369, 2003.

[21] M. Roessgen, A. Zoubir, and B. Boashash, "Seizure detection of newborn EEG using a model-based approach", *IEEE Transactions on Biomedical Engineering*, vol. 45, no. 6, pp. 673–685, 1998, ISSN: 0018-9294. DOI: 10.1109/10.678601.

[22] L. Rankine, N. Stevenson, M. Mesbah, and B. Boashash, "A nonstationary model of newborn EEG", *IEEE Transactions on Biomedical Engineering*, vol. 54, no. 1, pp. 19–28, 2007, ISSN: 0018-9294. DOI: 10.1109/TBME.2006.886667.

[23] P. Celka, B. Boashash, and P. Colditz, "Preprocessing and time-frequency analysis of newborn EEG seizures", *IEEE Engineering in Medicine and Biology Magazine*, vol. 20, no. 5, pp. 30–39, 2001, ISSN: 0739-5175. DOI: 10.1109/51.956817.

[24] B. Boashash, H. Carson, and M. Mesbah, "Detection of seizures in newborns using time-frequency analysis of EEG signals", in *Proceedings of the Tenth IEEE Workshop on Statistical Signal and Array Processing, 2000*, 2000, pp. 564–568. DOI: 10.1109/SSAP.2000.870188.

[25] B. Boashash, P. Colitz, and M. Mesbah, "Time-frequency detection of EEG abnormalities", in *Time-Frequency Signal Analysis and Processing: A Comprehensive Reference*, B. Boashash, Ed., Oxford, United Kingdom: Elsevier Ltd, 2003, pp. 663–670. [Online]. Available: http://eprints.qut.edu.au/21351/ (visited on 01/13/2014).

[26] *CDC - older adult falls - cost of fall injuries in older persons - figures 1-2 - home and recreational safety - injury center*, eng. [Online]. Available: http://www.cdc.gov/homeandrecreationalsafety/Falls/data/cost-estimates-figures1-2.html (visited on 03/17/2014).

[27] P. Kannus, "Fall-induced injuries and deaths among older adults", *Journal of the American Medical Association*, vol. 281, no. 20, pp. 1895–1899, 1999.

[28] *CDC - injury - WISQARS (web-based injury statistics query and reporting system)*. [Online]. Available: http://www.cdc.gov/injury/wisqars/index.html (visited on 09/10/2012).

[29] D. A. Skelton, C. A. Greig, J. M. Davies, and A. Young, "Strength, power and related functional ability of healthy people aged 65-89 years", *Age and Ageing*, vol. 23, no. 5, pp. 371–377, Sep. 1994, ISSN: 0002-0729. [Online]. Available: http://www.ncbi.nlm.nih.gov/pubmed/7825481 (visited on 09/10/2012).

[30] J. F. Bean, D. K. Kiely, S. Herman, S. G. Leveille, K. Mizer, W. R. Frontera, and R. A. Fielding, "The relationship between leg power and physical performance in mobility-limited older people", eng, *Journal of the American Geriatrics Society*, vol. 50, no. 3, pp. 461–467, Mar. 2002, ISSN: 0002-8614.

[31] J. M. Hausdorff, T. Herman, R. Baltadjieva, T. Gurevich, and N. Giladi, "Balance and gait in older adults with systemic hypertension", *The American Journal of Cardiology*, vol. 91, no. 5, pp. 643–645, Mar. 2003, ISSN: 0002-9149. [Online]. Available: http://www.ncbi.nlm.nih.gov/pubmed/12615286 (visited on 09/10/2012).

[32] M. Davis, *Blue in green*, 30th St Studio, New York City, New York, Aug. 1959.

[33] L. Cohen, *Time Frequency Analysis: Theory and Applications*, 1st. Prentice Hall, Dec. 1994, ISBN: 0135945321.

[34] J. O. Smith III, *Spectral Audio Signal Processing*, English. Stanford, Calif.: W3K Publishing, Dec. 2011, ISBN: 9780974560731.

[35] A. H. Nuttall, "Some windows with very good sidelobe behavior", *IEEE Transactions on Acoustics, Speech and Signal Processing*, vol. 29, no. 1, pp. 84–91, Feb. 1981, ISSN: 0096-3518. DOI: 10.1109/TASSP.1981.1163506.

[36] M. Abe and J. O. Smith, "Design criteria for simple sinusoidal parameter estimation based on quadratic interpolation of FFT magnitude peaks", English, Audio Engineering Society, Oct. 2004. [Online]. Available: http://www.aes.org/e-lib/browse.cfm?elib=12913 (visited on 04/23/2014).

[37] G. Sacco, F. Buchthal, and P. Rosenfalck, "Motor unit potentials at different ages", *Archives of Neurology*, vol. 6, pp. 366–373, 1962.

[38] S. M. Ling, R. A. Conwit, L. Ferrucci, and E. J. Metter, "Age-associated changes in motor unit physiology: observations from the baltimore longitudinal study of aging", *Archives of Physical Medicine and Rehabilitation*, vol. 90, no. 7, pp. 1237–1240, Jul. 2009, ISSN: 0003-9993. DOI: 10.1016/j.apmr.2008.09.565. [Online]. Available: http://www.sciencedirect.com/science/article/pii/S0003999308016936 (visited on 05/02/2014).

[39] D. M. R. Deschenes, "Effects of aging on muscle fibre type and size", en, *Sports Medicine*, vol. 34, no. 12, pp. 809–824, Oct. 2004, ISSN: 0112-1642, 1179-2035. DOI: 10.2165/00007256-200434120-00002. [Online]. Available: http://link.springer.com.pallas2.tcl.sc.edu/article/10.2165/00007256-200434120-00002 (visited on 05/02/2014).

[40] D. E. Vaillancourt, L. Larsson, and K. M. Newell, "Effects of aging on force variability, single motor unit discharge patterns, and the structure of 10, 20, and 40 hz EMG activity", *Neurobiology of Aging*, vol. 24, no. 1, pp. 25–35, Jan. 2003, ISSN: 0197-4580. DOI: 10.1016/S0197-4580(02)00014-3. [Online]. Available: http://www.sciencedirect.com/science/article/pii/S0197458002000143 (visited on 05/02/2014).

[41] R. M. Siervogel, A. F. Roche, J. H. Himes, W. C. Chumlea, and R. McCammon, "Subcutaneous fat distribution in males and females from 1 to 39 years of age.", en, *The American Journal of Clinical Nutrition*, vol. 36, no. 1, pp. 162–

171, Jul. 1982, ISSN: 0002-9165, 1938-3207. [Online]. Available: http://ajcn.nutrition.org/content/36/1/162 (visited on 02/16/2014).

[42] E. Blaak, "Gender differences in fat metabolism", eng, *Current opinion in clinical nutrition and metabolic care*, vol. 4, no. 6, pp. 499–502, Nov. 2001, ISSN: 1363-1950.

[43] A. E. J. Miller, J. D. MacDougall, M. A. Tarnopolsky, and D. G. Sale, "Gender differences in strength and muscle fiber characteristics", en, *European Journal of Applied Physiology and Occupational Physiology*, vol. 66, no. 3, pp. 254–262, Mar. 1993, ISSN: 0301-5548, 1439-6327. DOI: 10.1007/BF00235103. [Online]. Available: http://link.springer.com/article/10.1007/BF00235103 (visited on 02/16/2014).

[44] C. Bischoff, E. Stålberg, B. Falck, and K. E. Eeg-Olofsson, "Reference values of motor unit action potentials obtained with multi-MUAP analysis", en, *Muscle & Nerve*, vol. 17, no. 8, pp. 842–851, 1994, ISSN: 1097-4598. DOI: 10.1002/mus.880170803. [Online]. Available: http://onlinelibrary.wiley.com/doi/10.1002/mus.880170803/abstract (visited on 02/16/2014).

[45] M.-C. Chiu and M.-J. Wang, "The effect of gait speed and gender on perceived exertion, muscle activity, joint motion of lower extremity, ground reaction force and heart rate during normal walking", *Gait & Posture*, vol. 25, no. 3, pp. 385–392, Mar. 2007, ISSN: 0966-6362. DOI: 10.1016/j.gaitpost.2006.05.008. [Online]. Available: http://www.sciencedirect.com/science/article/pii/S0966636206000993 (visited on 03/06/2014).

[46] R. Ferber, I. McClay Davis, and D. S. Williams III, "Gender differences in lower extremity mechanics during running", *Clinical Biomechanics*, vol. 18, no. 4, pp. 350–357, May 2003, ISSN: 0268-0033. DOI: 10.1016/S0268-0033(03)

00025-1. [Online]. Available: http://www.sciencedirect.com/science/article/pii/S0268003303000251 (visited on 03/06/2014).

[47] J. Rose and J. G. Gamble, *Human Walking*, en. Lippincott Williams and Wilkins, 2006, ISBN: 9780781759540.

[48] S. Manek and M. F. Lew, "Gait and balance dysfunction in adults", ENG, *Current treatment options in neurology*, vol. 5, no. 2, pp. 177–185, Mar. 2003, ISSN: 1092-8480.

[49] J. Dumurgier, A. Elbaz, C. Dufouil, B. Tavernier, and C. Tzourio, "Hypertension and lower walking speed in the elderly: the three-city study:" en, *Journal of Hypertension*, vol. 28, no. 7, pp. 1506–1514, Jul. 2010, ISSN: 0263-6352. DOI: 10.1097/HJH.0b013e328338bbec. [Online]. Available: http://journals.lww.com/jhypertension/Abstract/2010/07000/Hypertension_and_lower_walking_speed_in_the.24.aspx (visited on 04/28/2014).

[50] A. De Stefano, J. H. Burridge, V. T. Yule, and R. Allen, "Effect of gait cycle selection on EMG analysis during walking in adults and children with gait pathology", *Gait & Posture*, vol. 20, no. 1, pp. 92–101, Aug. 2004, ISSN: 0966-6362. DOI: 10.1016/S0966-6362(03)00099-7. [Online]. Available: http://www.ncbi.nlm.nih.gov/pubmed/15196526 (visited on 09/10/2012).

[51] J. W. Youdas, J. H. Hollman, M. J. Aalbers, H. N. Ahrenholz, R. A. Aten, and J. J. Cremers, "Agreement between the GAITRite walkway system and a stopwatch-footfall count method for measurement of temporal and spatial gait parameters", eng, *Archives of physical medicine and rehabilitation*, vol. 87, no. 12, pp. 1648–1652, Dec. 2006, ISSN: 0003-9993. DOI: 10.1016/j.apmr.2006.09.012.

[52] J. L. McGinley, R. Baker, R. Wolfe, and M. E. Morris, "The reliability of three-dimensional kinematic gait measurements: a systematic review", *Gait &*

Posture, vol. 29, no. 3, pp. 360–369, Apr. 2009, ISSN: 0966-6362. DOI: 10.1016/j.gaitpost.2008.09.003. [Online]. Available: http://www.sciencedirect.com/science/article/pii/S0966636208002646 (visited on 04/28/2014).

[53] P. Mitchell, D. Krotish, Y.-J. Shin, and V. Hirth, "Cross time-frequency analysis of gastrocnemius electromyographic signals in hypertensive and nonhypertensive subjects", en, *EURASIP Journal on Advances in Signal Processing*, vol. 2010, no. 1, p. 206 560, Aug. 2010, ISSN: 1687-6180. DOI: 10.1155/2010/206560. [Online]. Available: http://asp.eurasipjournals.com/content/2010/1/206560 (visited on 09/10/2012).

[54] C. J. De Luca, L. D. Gilmore, M. Kuznetsov, and S. H. Roy, "Filtering the surface EMG signal: movement artifact and baseline noise contamination", eng, *Journal of biomechanics*, vol. 43, no. 8, pp. 1573–1579, May 2010, ISSN: 1873-2380. DOI: 10.1016/j.jbiomech.2010.01.027.

[55] C. J. De Luca, M. Kuznetsov, L. D. Gilmore, and S. H. Roy, "Inter-electrode spacing of surface EMG sensors: reduction of crosstalk contamination during voluntary contractions", eng, *Journal of biomechanics*, vol. 45, no. 3, pp. 555–561, Feb. 2012, ISSN: 1873-2380. DOI: 10.1016/j.jbiomech.2011.11.010.

[56] Delsys, "Technical note 101 - EMG sensor placement", Delsys, Inc., Technical Note, 2012. [Online]. Available: http://www.delsys.com/Attachments_pdf/TN101%20-%20EMG%20Sensor%20Placement-web.pdf (visited on 06/01/2014).

[57] M. Folstein, S. Folstein, and P. McHugh, "Mini mental state examination", *Psychological Assessment Resources (PAR)*, 1975.

[58] H. Eberhart, V. Inman, and B. Bresler, "The principal elements in human locomotion", in *Human Limbs and Their Substitutes*, P. Klopsteg and P. Wilson, Eds., New York: Mcgraw-Hill, 1954.

[59] A. J. Campbell, J. Reinken, B. C. Allan, and G. S. Martinez, "Falls in old age: a study of frequency and related clinical factors", *Age and Ageing*, vol. 10, no. 4, pp. 264–270, Nov. 1981, ISSN: 0002-0729. [Online]. Available: http://www.ncbi.nlm.nih.gov/pubmed/7337066 (visited on 09/10/2012).

[60] F. E. Grubbs, "Procedures for detecting outlying observations in samples", *Technometrics*, vol. 11, no. 1, pp. 1–21, 1969, ISSN: 0040-1706. DOI: 10.1080/00401706.1969.10490657. [Online]. Available: http://www.tandfonline.com/doi/abs/10.1080/00401706.1969.10490657 (visited on 08/05/2013).

[61] T. Oberg, A. Karsznia, and K. Oberg, "Basic gait parameters: reference data for normal subjects, 10-79 years of age", eng, *Journal of rehabilitation research and development*, vol. 30, no. 2, pp. 210–223, 1993, ISSN: 0748-7711.

[62] P. Bonato, P. Boissy, U. Della Croce, and S. Roy, "Changes in the surface EMG signal and the biomechanics of motion during a repetitive lifting task", *IEEE Transactions on Neural Systems and Rehabilitation Engineering*, vol. 10, no. 1, pp. 38–47, 2002, ISSN: 1534-4320. DOI: 10.1109/TNSRE.2002.1021585.

[63] H. Huang, J. He, R. Herman, and M. Carhart, "Modulation effects of epidural spinal cord stimulation on muscle activities during walking", *IEEE Transactions on Neural Systems and Rehabilitation Engineering*, vol. 14, no. 1, pp. 14–23, 2006, ISSN: 1534-4320. DOI: 10.1109/TNSRE.2005.862694.